Enhanced Gas Migration Through Permeable Bubble Networks Within Consolidated Soft Sediments

Michael Johnson
School of Chemical and Process Engineering, University of Leeds, Leeds LS2 9JT, U.K

Jeffrey Peakall
School of Earth and Environment, University of Leeds, Leeds LS2 9JT, U.K

Xiaodong Jia and Michael Fairweather
School of Chemical and Process Engineering, University of Leeds, Leeds LS2 9JT, U.K

David Harbottle and Simon Biggs
School of Chemical Engineering, University of Queensland, Brisbane, QLD 4072, Australia

Timothy N. Hunter*
School of Chemical and Process Engineering, University of Leeds, Leeds LS2 9JT, U.K

DOI 10.1002/aic.16223
Published online August 20, 2018 in Wiley Online Library (wileyonlinelibrary.com)

Many consolidated sediments experience in situ gas generation from methanogenesis, corrosion, or radiolysis reactions and can retain bubbles for long periods. Particular interest is motivated by the retention and acute release of flammable hydrogen from nuclear legacy waste sludge. X-ray computed tomography was employed to observe 0.07–10 mm bubble populations within 30–1112 Pa yield strength $Mg(OH)_2$ sediments. High rates of partial coalescence were observed among sub-millimeter microvoids, forming extensive bubble networks which spanned the 32 mm field of view. Lattice Boltzmann and Monte Carlo modeling demonstrated these networks to be highly pervious to gas, with effective diffusivities for hydrogen of 3.7–12.5 $\times 10^{-5}$ m^2 s^{-1}. Continuous vessel-spanning bubble networks, dynamic connectivity between ganglia of coalesced bubbles, Haines jumps, and composite diffusion through the gas and aqueous phase can account for enhanced gas migration over length-scales of several meters, thus enabling chronic gas release from low-intermediate strength sediments ($10\,\mathrm{Pa} \lesssim \tau \lesssim 1$ kPa) too strong for buoyant bubble ebullition and too weak for vertical channel formation. *AIChE J*, 64: 4131–4147, 2018
Keywords: bubble, x-ray tomography, sludge, Monte Carlo, diffusion

Introduction

Many natural water systems, including shallow marine beds,[1,2] lakes,[3,4] rivers,[5] and wetlands,[6] experience *in situ* gas generation, retention, and release as a result of methanogenesis, contributing significantly to global greenhouse gas emissions.[3,7] Conversely, biogenic methane generation can be effectively exploited for commercial biogas production from the anaerobic digestion of wastewater sludges, thereby offsetting the economic and carbon costs of treatment,[8] while the trapping of gas within deep saline sedimentary formations remains a promising option for geological carbon sequestration.[9] The presence of gas bubbles has also provoked research into their impact on the bulk strength and elasticity of marine sediments due to the significant implications for the offshore construction industry.[10] Legacy nuclear waste *sludge* deposits, for example, at Sellafield, UK[11] and Hanford, USA,[12,13] also experience *in situ* gas (mainly hydrogen) generation due to corrosion of metallic cladding materials and exposed fuel elements, combined with radiolysis of aqueous liquors by water soluble fission products. Further understanding of gas migration and chronic release is required to mitigate against acute gas release events[13,14] with the potential to present a flammability hazard which could risk a breach of containment.

A number of chronic gas release mechanisms have been proposed. Some release of dissolved volatiles from the continuous phase at the bed surface will occur, although 98% of methane release from shallow lakes reportedly originates from free, rather than dissolved gas.[7] Buoyant rise of individual bubbles, or *ebullition*, has been suggested for relatively low yield stress soft sediments[4,15] considered unlikely to exhibit the mechanical strength to withstand the buoyant stress at the shallow surface of the bubble. However, bubble ebullition in natural sediments is typically triggered by wind,[3] with a negligible methane flux observed under stagnant, or quiescent,

Correspondence concerning this article should be addressed to T.N. Hunter at t.n.hunter@leeds.ac.uk.

conditions more typical of nuclear waste silos. Relatively modest yield stresses[15] are required to resist the buoyant stress of the <20 mm bubbles typical within consolidated soft sediments.[11,14] Sherwood and Eduardo Sáez[14] suggested that bubble ebullition, possibly liberating a buoyant flux, or cascade, of bubbles is most likely in the $3 < \tau < 70$ Pa yield stress range.

An alternative gas release mechanism was proposed whereby retained bubbles of a critical length can propagate upwards by preferentially fracturing the sediment at the shallow surface and closing at the tail, thus appearing to *burrow* vertically through the sediment.[6,16] Fracture toughness typically diminishes with increased yield stress[17] promoting burrowing within highly consolidated sediments of kiloPascal scale yield stress. Furthermore, another x-ray tomography study by the current authors[11] observed that the largest, most mature bubbles remain static on time-scales of several hours during periods of appreciable chronic gas release from sediments of 7–1112 Pa, implying the existence of a gas release mechanism spanning a broad range of shear yield stress conditions which does not entail macroscopic migration of large individual bubbles. A succession of small *partial rollover* events[18] was briefly considered to explain the chronic gas release, whereby a region of sediment with a high voidage of sub-millimeter bubbles breaks free of the surrounding bulk material and rises through the bed, however no characteristic disturbances in topography or profile of the bed were apparent from tomographic imaging.[11] Thus, the established mechanisms for gas migration cannot account for chronic release from low-medium ($\approx 10\,\text{Pa} < \tau < \text{kPa}$) yield stress conditions, sufficient in strength to resist ebullition but insufficient in stress to support deep drainage channels or enable burrowing. It was postulated by Johnson et al.[11] that permeable networks of partially coalesced sub-millimeter bubbles or diffusion pathways through fine fractures,[4] often below the detection limit of large scale clinical tomography, might offer a more realistic explanation for gas migration and chronic release. Similarly, Wheeler[2] highlighted the possibility that retained free gas within unsaturated soils may be continuous at large void fractions where the *saturation*, given by the ratio of the pore water volume to the combined volumes of pore water and retained gas, falls below a value of around 0.85. However, x-ray computed tomography (CT) has yet to be employed to observe viable pathways for gas migration through these intermediate strength quiescent sediments.

In this study, gas retention is investigated by the homogeneous *in situ* decomposition of hydrogen peroxide within consolidated $Mg(OH)_2$ soft sediments of 30–1112 Pa yield stress, using a Siemens Inveon PET/CT scanner[19] to image the bubble population at 53.25 μm resolution. Previous research into sedimentary bubbles achieving such tomographic imaging resolution has focused on individual fracture sites propagated from a solitary submerged orifice,[1,6,20] while the larger scale studies of diverse bubble populations[11,21] have been limited by spatial resolution, rendering communication between multiple bubble sites and avenues for gas migration invisible. The sediment response to *in situ* bubble growth is interpreted in relation to the two-phase sediment microstructure, which is characterized using low field nuclear magnetic resonance (LFNMR) spectroscopy[22,23] and cryogenic focused ion beam (cryo-FIB) microscopy. X-ray CT is coupled to lattice Boltzmann method (LBM) and Monte Carlo based simulations, which are proposed for the investigation of gas migration through permeable, connected pathways through the sediment. These computational approaches are highly suitable for characterizing flow behavior through real porous media as they are computationally inexpensive compared with conventional continuum-based computational fluid dynamics (CFD) methods for complex boundary geometries, while the CT reconstructions provide a compatible cubic *lattice* on which to perform the calculations.[24]

Materials and Methods

Test materials

A dry commercial $Mg(OH)_2$ powder, Versamag (Martin Marietta Magnesia Specialties LLC, USA),[11] was used as a non-active analogue for the solid component of the brucite-rich[25,26] corroded Magnox sludge (CMS) stored at Sellafield. Water was added to the $Mg(OH)_2$ powder prior to agitation for 30 min using an overhead stirrer with an axial flow impeller in order to provide homogeneous soft sediments in the 35–54% w/w concentration range. Versamag has a laser diffraction measured median particle size of 3–4 μm,[26] while its soft sediments exhibit yield stresses as a function of solids concentration, ω, given by $\tau = 2.156 \times 10^5 \omega^{8.55}$.[11] 35, 45, and 54% w/w sediments were prepared for x-ray tomography imaging, corresponding to diverse shear yield stress conditions of 30, 234, and 1112 Pa, respectively.

Soft sediment microstructure characterization

The soft sediment microstructure was investigated using a combination of LFNMR spectroscopy, mercury intrusion porosimetry (MIP), and cryo-FIB imaging. LFNMR has proven to be a powerful and non-destructive tool for characterizing various porous media, including tight gas sandstones[27] and different grades of coal.[23] Following application of a very low external magnetic field, transverse relaxation time (T_2) measurements capture the rate at which protons in the pore filling fluid, water in this instance, lose their magnetic *spin* as a result of collision with the pore walls. Hence, LFNMR can non-destructively probe the pore surface area to volume ratios, *S*/*V*, a measure of inverse pore body radius, r_{pb}^{-1}, within water saturated porous materials, such as sludges, slurries, and soft sediments. From the resulting transverse relaxation time distribution, slower proton relaxation times correspond to fewer pore wall interactions, consistent with larger pore bodies according to Eq. 1[22,23]

$$\frac{1}{T_2} = \rho_2 \frac{S}{V} \tag{1}$$

Translating the relaxation time distribution into a pore size distribution therefore requires the determination of a material dependent proportionality constant, ρ_2, representing the transverse relaxation strength. In order to calibrate the transverse relaxation strength a 20 mL sample of soft sediment was dried for 24 h at 100°C to form a 30 mm diameter disk which was cut into two halves. One half was then re-saturated with water for 24 h before LFNMR analysis, while the other half was analyzed using MIP.

Mercury intrusion porosimetry uses an applied external pressure to force a non-wetting fluid, mercury, to intrude into a porous sample. The Washburn equation, Eq. 2, states that the applied pressure, *P*, required for the non-wetting fluid to invade a pore, with an assumed cylindrical geometry, is inversely proportional to the pore throat radius, r^{th}

$$r^{\text{th}} = \frac{2\sigma\cos(\theta)}{P} \approx \frac{0.62}{P} \tag{2}$$

For any material which is poorly wetted by mercury the numerator of Eq. 2 will be equivalent. A mercury vapour-air surface tension, σ, of 485 mN m^{-1} and a high three phase contact angle of 130°C are typically used for such advancing or intruding experiments.[28] The percentage intrusion into the dried sample during an incremental sweep of applied external pressures can thereby be translated into a distribution of pore throat radii for comparison with the LFNMR distribution for the dried and re-saturated sample. Comparison of the distinctive LFNMR and MIP modes[29] enables conversion of transverse relaxation times to a more relevant pore length-scale. The ratio of MIP determined modal pore throat radius to LFNMR determined modal relaxation time provides the product of the transverse relaxation strength and the pore throat to body ratio, henceforth referred to as a corrected transverse relaxation strength, $\rho_{2,\text{cor}}$, according to Eq. 3

$$\frac{2\sigma\cos(\theta)}{\overline{PT_2}} = \rho_2 \overline{r}^{\text{th}} \left(\frac{\overline{S}}{V}\right) = \rho_2 \frac{\overline{r}^{\text{th}}}{\overline{r}_{\text{pb}}} = \rho_{2,\text{cor}} \tag{3}$$
$$r^{\text{th}} = \rho_{2,\text{cor}} T_2$$

The corrected transverse relaxation strength will be constant only if the pore bodies and throats scale with a fixed ratio, however discrete element method analysis of compacted sands and soils indicates that this assumption is reasonable.[30] Following Eq. 3 the corrected transverse relaxation strength translates the relaxation time distribution into a more useful pore throat size distribution. Following determination of the corrected transverse relaxation strength using the dried samples, LFNMR analysis was performed using 50 mL samples of 35–54% w/w magnesium hydroxide soft sediments.

The MIP tests were conducted using a 413 MPa Autopore IV porosimeter[27] (Micromeritics, USA) by increasing the applied pressure from 10 kPa to 413 MPa ceiling in 42 logarithmic stages and recording the mass of mercury intrusion at each interval. LFNMR was undertaken using a MARAN Ultra benchtop NMR analyser[31] (Oxford Instruments, UK) operated with 100 scans per sample, to ensure an adequate signal to noise ratio, a magnetic field strength of 0.047 T and 2 MHz resonance frequency. Further measurement specifications include an echo spacing of 100 μs, echo numbers of 4096 and an equilibrium time of 10 s between scans. The resulting echo data were inverted to relaxation times in the 0.1–10000 ms range with 100 logarithmically spaced intervals.

To supplement the LFNMR and MIP data with an appreciation of the pore geometry, a 40% w/w $Mg(OH)_2$ soft sediment sample was observed using cryo-FIB imaging. The sample was rapidly frozen by quenching with slush nitrogen before the temperature was increased to and maintained at −90°C for 8 min in order to sublime away the majority of the pore-water. The frozen and sublimed sample was then fractured and sputter coated with platinum for the topography to be imaged using a Helios G4 CX DualBeam microscope (FEI, USA).[32,33] Images were acquired of the topography of the fractured surface and the interior wall of a borehole etched from the sample by the FIB, or FIB cross-section.

Imaging gas retention within soft sediments with x-ray computed tomography

Gas retention tests were conducted in accordance with the hydrogen peroxide decomposition method outlined in Johnson et al.,[11] within a smaller sideways mounted acrylic cylinder of 71 mm diameter and 138 mm length; using a cylindrical sample ensured a constant x-ray path length through the medium and thus relatively uniform x-ray attenuation through the sediment.[34] *In situ* gas generation was achieved by the addition of 1.6 mL 35% w/w hydrogen peroxide (Merck Chemicals, Germany) to a 360 mL volume of soft sediment and agitation for 10 min with an overhead stirrer before transfer to the test cylinder. Following 6 h of gas generation, producing 220 mL O_2 by Eq. 4, the bed was deemed to have reached a steady state voidage, or maximum gas *holdup*, and bubble size distribution (BSD) based on the larger scale tests in Johnson et al.[11]

$$H_2O_2 \rightarrow H_2O + \frac{1}{2}O_2 \tag{4}$$

Computed tomography scans were undertaken for three commercial magnesium hydroxide soft sediments of 35, 45, and 54% w/w using an Inveon dual positron emission tomography (PET)/CT scanner (Siemens, Germany). Operating in tomography mode, the Inveon scanner provided an 80 kV, 500 μA *cone-beam* x-ray source from a tungsten anode with a focal spot size of <50 μm. The x-ray source, mounted opposite a camera with detectors spaced at 32 μm, rotates around the static sample capturing projections at 1°C angles through 180°C before the projections are reconstructed to achieve the imaging parameters outlined in Table 1. The 53.25 μm voxel resolution captured 4.7–9.1 times more detail in the cross-sectional plane and 11.7–23.5 times more detail in the axial direction than the large clinical CT tests conducted in Johnson et al.,[11] albeit at the expense of a significantly longer scan duration in the order of 20 min.

X-ray CT post processing

The reconstructed x-ray tomographs were post processed using FIJI ImageJ[35] in combination with DigiUtility (Structure Vision Ltd., UK).[36] A $600 \times 600 \times 600$ voxel representative cubic sub-sample was extracted from the center of the image stack, away from the test-cylinder walls and dispensing with the outermost slices which demonstrated reduced CT-numbers, consistent with a cupping artefact due to x-ray scatter interference.[37] Various techniques including bandpass filtering, sharpening, and despeckling were then used to suppress ring-artefacts[38,39] and reduce *speckling* noise caused by beam hardening.[40] Bilevel thresholding was then used to isolate the retained bubble population from the high radiodensity bulk sediment. From the thresholded image stack, each object with face, edge and corner connected voxels was extracted, labeled and its volume recorded using the algorithm outlined in Bolte and

Table 1. Summary of X-Ray CT Scanning Parameters and Comparison with the Scanning Protocol Used in Johnson et al.[11]

	Siemens Inveon PET/CT	GE Brivo CT385[11]
X-ray voltage (kVp)	80	120
X-ray tube current (mA)	0.5	40–79
Scan duration (s)	≈1000	<1.1
Field of view diameter (mm)	81.8	96–250
Pixel resolution (μm)	53.25	250–488
Slice separation (μm)	53.25	625–1250
Number of axial slices	1024	32–112
Field of view volume (μm^3)	2.86×10^5	1.40×10^5–6.81×10^6

Cordelières.[41] These objects include any discrete bubbles retained by the sediment as well as any chains or networks of partially coalesced bubbles which might propagate through the volume.

Characterizing partially coalesced or networked bubbles

Where high rates of *partial bubble coalescence* or networks of bubbles are observed, an additional approach is required to characterize the individual bubbles within the network. Automated watershed segmentation is often used for isolating touching objects within digital images; however, this approach is best applied for overlapping objects of narrow size and shape distributions which are atypical for bubbles retained by consolidated soft sediments.[42,43] Instead a *mean empty space* (MES) algorithm was used whereby 10^8 random points were selected within the thresholded void-space and the lengths of three perpendicular chords (in the x, y, and z directions) through each of these loci to the nearest sediment boundaries were recorded, providing a comprehensive chord length distribution (CLD) of the individual bubble population within the domain. The discretized CLDs were then translated into BSDs by solving the chord length transformation matrix from Li and Wilkinson[44] using the non-negative least squares (NNLS) algorithm from Lawson and Hanson[45] in Matlab v. R2013b (Mathworks, USA); the discretised BSDs were smoothed using a three point moving average to reduce some of the noise in the NNLS solution.

Simulating gas transport through permeable bubble networks

Two alternative three-dimensional computational approaches were employed to characterize gas transport behavior through soft sediments using the bi-level thresholded CT reconstructions; these are the LBM and Monte Carlo gas diffusion (MCGD) models outlined below. For analyzing one-directional gas transport, a $400 \times 400 \times 400$ voxel CT volume was encased in a solid duct with walls at the boundaries normal to the direction of the pressure or concentration gradient. All simulations were performed using a 3 GHz CPU Intel i5 processor with 2 × 8 Gb RAM.

Lattice Boltzmann method

Lattice Boltzmann method represents an alternative numerical scheme to conventional continuum-based CFD methods for simulating fluid flow. While conventional CFD provides numerical solutions to the Navier-Stokes equations at the continuum level, LBM represents the fluid as discrete particles using microscopic collision models and kinetic equations ultimately recovering a continuum solution for macroscopic fluid properties, such as the fluid density, ρ, and superficial fluid velocity, u. A number of studies[24,46,47] have married x-ray CT structures with LBM simulations to predict the hydraulic properties of porous media as LBM is computationally inexpensive in comparison to conventional CFD approaches for systems with complex boundary geometries, while the computational lattice nodes at which flow behavior is resolved are easily mapped onto the domain of cubic voxels generated during CT reconstruction.[24]

Lattice Boltzmann method simulations were performed using DigiFlow (Structure Vision Ltd., UK), based on a D3Q19 cubic lattice structure[36,48,49] demonstrated in Figure 1,[49] whereby particles at the central node of a local $3 \times 3 \times 3$ cubic lattice interact with 18 of their 26 nearest neighbors (excluding the eight extreme corners of the lattice). Each lattice node is thereby associated with 18 mass probability functions (MPFs), $f(x,t,e_i)$, which represent the number of particles with a particular velocity vector, e_i, at a position, x, and time, t.

Particles collide and propagate through the domain, redistributing MPFs between lattice nodes according to the models summarized in Figure 1. Collisions are governed by the Bhatnagar–Gross–Krook (BGK) model,[50] where a user defined relaxation constant, $\boldsymbol{\tau}$, dictates the rate at which the MPF decays toward the equilibrium value. The relaxation constant relates to the kinematic viscosity of the fluid, $\hat{\boldsymbol{\nu}}$, according to Eq. 5, where the circumflex accent denotes the dimensionless form of the variable used within the LBM simulation

$$\tau = 2\hat{\boldsymbol{\nu}} - 1 \quad (5)$$

Fluid particle interactions at the solid boundaries are governed by a no-slip boundary condition whereby the MPF is returned to its pre-collision lattice node with a velocity vector equal in magnitude and opposite in direction.[51] The MPFs also

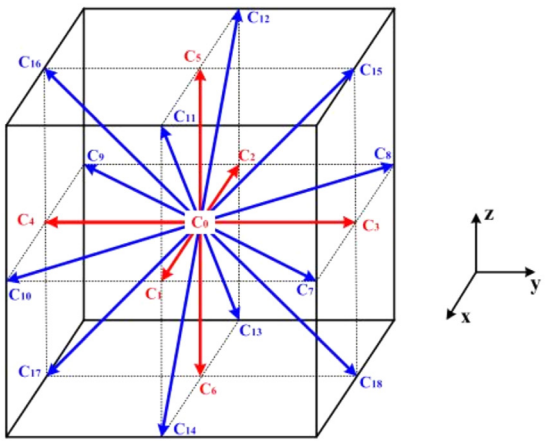

MPF propagation

$$f_i(x + e_i\delta_t, t + \delta_t) = f_i(x,t)$$

Fluid-solid collisions (no-slip)

$$f^*_{-i}(x, t + \delta_t) = f_i(x,t)$$

Fluid-fluid collisions (BGK model)

$$f^*_i(x,t) = f_i(x,t) - \tfrac{1}{\tau}\left(f_i(x,t) - f^{eq}_i(x,t)\right)$$

$$f^{eq}_i(x,t) = \omega_i \hat{\rho}\left[1 + 3e_i\hat{u} + \tfrac{9}{2}(e_i\hat{u})^2 - \tfrac{3}{2}\hat{u}^2\right]$$

where $\omega_i = \tfrac{1}{3}, \tfrac{1}{16}, \tfrac{1}{36}$ for $i = 0, 1-6, 7-18$

Figure 1. Schematic of the D3Q19 lattice structure (left), reproduced from Guan et al.,[49] and a summary of the governing *propagation*[49] and *collision*[50,51] models which redistribute the MPFs at each computational time step.

[Color figure can be viewed at wileyonlinelibrary.com]

propagate between neighboring fluid lattice nodes according to their velocity vectors.[49] The macroscopic fluid density, $\hat{\rho}$, and velocity, $\hat{u}$ are derived from the MPFs and their associated velocity vectors according to Eq. 6

$$\hat{\rho} = \sum_{1}^{19} f_i$$
$$\hat{u} = \frac{1}{\hat{\rho}} \sum_{1}^{19} e_i f_i + \boldsymbol{\tau} \frac{\hat{\boldsymbol{L}}}{\Delta \hat{P}} \tag{6}$$

All LBM calculations are performed in dimensionless lattice units (LU), where distance is reported in terms of lattice cell width, $\delta_x = 1$, and time in terms of computational time steps, $\delta_t = 1$. Length scales are easily translated into physical units as the lattice cells have the dimensions of the CT voxel resolution ($\Delta x = 5.325 \times 10^{-5}$ m). The computational time step can be derived in physical units as the virtual and physical environments share a common Reynolds number, enabling conversion between virtual and physical velocities using the lattice width, relaxation constant, and kinematic viscosity of the permeating fluid, as shown in Eq. 7

$$\left(\frac{u \Delta x}{\nu}\right) = \left(\frac{\hat{u} \delta x}{\hat{\nu}}\right)$$
$$\frac{u}{\hat{u}} = \frac{\Delta x}{\Delta t} = \frac{\nu \delta x}{\hat{\nu} \Delta x} \tag{7}$$
$$\Delta t = \frac{\Delta x^2 (2\tau - 1)}{6\nu}$$

For a relaxation constant of unity and a kinematic viscosity for oxygen of 2.04×10^{-5} m^2 s^{-1}, a computational iteration corresponds to 2.32×10^{-5} s in real time. A small pressure gradient, $\nabla \hat{P} = \Delta \hat{P} / \hat{L}$, of 2.5×10^{-4} LU, equivalent to 1.65 Pa m^{-1}, was prescribed to induce flow in a desired direction and LBM simulations were run until the superficial velocity of fluid through a cross-section of the domain, including all fluid and solid sites, achieved steady state. The pressure gradient, superficial velocity, and fluid viscosity are then used to predict the permeability of the void-space, κ, in m^2 according to Darcy's Law, as shown in Eq. 8[24,51]

$$\kappa = \Delta x^2 \frac{\hat{u} \hat{\nu} \hat{L} \hat{\rho}}{\Delta \hat{P}} \tag{8}$$

where $\hat{L}$ is the width of the domain in voxels.

Monte Carlo gas diffusion

Monte Carlo gas diffusion simulations were performed using DigiDiffuse software (Structure Vision Ltd., UK), based on a model originally developed for aggregation and sedimentation research.[52] following a number of studies[53-56] that have employed Monte Carlo style simulations to imitate the seemingly random nature of molecular diffusion within complex porous structures. Here, the simulation domain was constructed of source, porous medium and sink regions each 400 voxel 'or 21.3 mm' wide. The source region, $x =$ 0–400 voxel, is charged with a fixed concentration, ϕ_s, of *tracer* particles. Tracer particles diffuse through the porous medium, x = 400–800 voxel, where tracer molecule concentrations in the void-space, $\phi(x,t)$, increase over time and decay with distance. Tracer particles which pass through the permeable void-space then accumulate in the enclosed sink region, x = 800–1200 voxel. Tracer concentrations are taken to be the number of molecules, $\#_M$, per unit volume of void-space, in order to provide a continuous concentration profile through every region of the domain in spite of sudden expansions and constrictions. The concentration within the porous region should therefore be multiplied by the void fraction in order to determine the concentration of oxygen tracers within the entire cubic volume.

In order to mimic macroscopic gas migration, tracer particles are able to randomly move to any of the 26 immediately adjacent sites as long as that site is not occupied by another tracer particle or a solid boundary. Thus, in contrast to the LBM simulations, the propagation of fluid particles exhibits no dependence on previous computational steps, only the current location of tracer particles. In the highly improbable instance that every adjacent lattice site is occupied, the move is rejected for that iteration of the simulation, implying that the net effect of all collisions during that computational iteration return the particle to its pre-collision lattice node. The rejection of particle transfer to occupied sites thereby promotes macroscopic diffusion along the direction of the concentration gradient. The evolution in concentration with time relates to the concentration gradient according to Fick's second law of diffusion, the linear form of which is given in Eq. 9

$$\frac{d\phi}{dt} = D \frac{d^2 \phi}{dx^2} \tag{9}$$

where D is the diffusivity, or effective diffusivity, D_{eff} in the case of a porous medium with tortuous diffusion paths. A common analytical solution to Eq. 9 is defined in Eq. 10[56,57] for the boundary conditions of (a) constant source concentration within a plane at $x = 0$, $\phi(0,t) = \phi_0$, and (b) zero concentration infinitely far from the source, $\phi(\infty, t) = 0$

$$\phi(x,t) = \phi_0 \operatorname{erfc}\left(\frac{x}{2\sqrt{Dt}}\right)$$
$$\operatorname{erfc}\left(\frac{x}{2\sqrt{Dt}}\right) = 1 - \frac{2}{\sqrt{\pi}} \int_0^{\frac{x}{2\sqrt{Dt}}} \exp(-\xi^2) d\xi \tag{10}$$

where erfc is the complement, 1−erf, to the Gaussian error function (erf). Alternatively, for a source region, $0 \le x \le h$, maintained at a constant average concentration, ϕ_s, by replenishing tracer particles at $x = 0$, and a solid wall at the end of the finite volume, $x = L$, the concentration throughout the domain is better represented using Eq. 11[57]

$$\phi(x,t) = \frac{\phi_s A}{B}$$
$$A = \frac{1}{2}\left(\operatorname{erfc}\left(\frac{x-h}{2\sqrt{Dt}}\right) - \operatorname{erfc}\left(\frac{x+h}{2\sqrt{Dt}}\right) + \operatorname{erfc}\left(\frac{2L-h-x}{2\sqrt{Dt}}\right)\right) \tag{11}$$
$$B = \frac{1}{h} \int_0^h A \, dx$$

where the integral of A across the width of the source region in the denominator ensures that the bulk concentration of tracer particles in the source region remains constant, at ϕ_s. The third term in square brackets captures the reflection and superposition of particles colliding with the boundary at $x = L$. For an assumed diffusivity, these two analytical solutions provide a mathematical basis to predict the evolution in tracer concentration through time and space in line with the MCGD simulations; the observed diffusivity for each porous medium is found where there is best agreement between the simulated, $\hat{\phi}(x,t)$, and analytical, $\phi(x,t)$, solutions, quantified by the minimum total absolute error across the width of the porous region

$$D = D_{\text{eff}} \text{ when } E \rightarrow \text{minimum where :}$$
$$E = \sum_{t=1\times10^{3}\text{step}}^{5\times10^{5}} \sum_{x=400\text{voxel}}^{800} |\sim\phi(x,t) - \phi(x,t)| \qquad (12)$$

In the case of an open duct, with no geometric obstacles to diffusion, the diffusivity will correspond to the *self-diffusion coefficient*, which are known to be 1.92×10^{-5} m^2 s^{-1} and 1.60×10^{-4} m^2 s^{-1} for oxygen[58] and hydrogen[59] respectively. Thus, diffusion through an open duct can be used to calibrate the duration of a computational time step, Δt, in order to translate the effective diffusivities into physical units.

Results and Discussion

Soft sediment microstructure

Mercury intrusion into half a dried disk of $Mg(OH)_2$ is presented in Figure 2a beside a LFNMR transverse relaxation time distribution for the other half of the dried disk, following re-saturation with water, in Figure 2b. 80% of the pore-space is intruded by mercury between applied pressures of 2.1–30.9 MPa; applying the Washburn equation, with an advancing contact angle of 130°C,[28] the center of this mode corresponds to a pore throat radius of 0.087 μm.

Similarly, the transverse relaxation time distribution demonstrates a distinct mode centered around T_2 = 12.3 ms. The ratio of the MIP determined modal pore throat radius and the modal relaxation time yields a corrected transverse relaxation strength of 7×10^{-6} m s^{-1}, which is hereafter used to translate relaxation time data into pore throat size distributions for wet soft sediments.

Mercury intrusion porosimetry and LFNMR derived pore size distributions for the dried samples and three $Mg(OH)_2$ soft sediments are presented in Figure 3. The distributions are normalized to probability density, $p(r_{th})$, values, given by Eq. 13, whereby the area under each curve is unity and so narrower size distributions manifest with taller peaks

$$\int_0^{\infty} p(r^{\text{th}})\, \mathrm{d}\, log_{10}(r^{\text{th}}) = 1 \qquad (13)$$

From Figure 3, it is apparent that consolidating soft sediments results in constriction of the sedimentary pores,

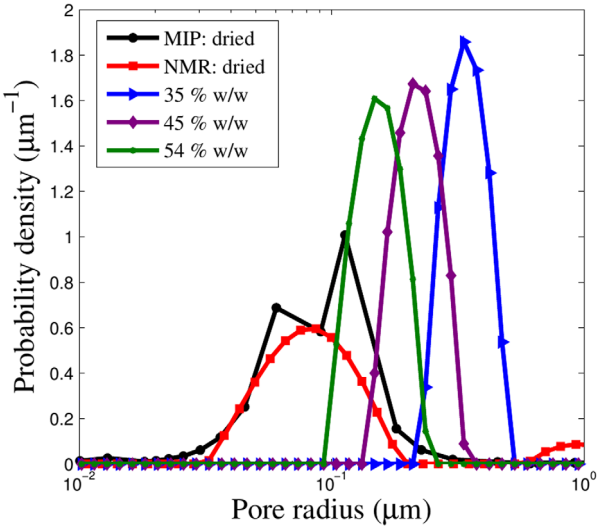

Figure 3. Pore throat size distributions for $Mg(OH)_2$ soft sediments of 35–54% w/w solids concentration obtained by low-field nuclear magnetic resonance spectroscopy with a mercury intrusion porosimetry calibrated *corrected transverse relaxation strength.*

[Color figure can be viewed at wileyonlinelibrary.com]

however consolidation enhances the shear yield stress much more significantly than it constricts the pore throat radii. Increasing the solids concentration from 35 to 54% w/w sees the modal pore throat radius decrease from 0.335 to 0.148 μm, while the yield stress increases by nearly two orders of magnitude, from 30 to 1112 Pa.

Each of the three $Mg(OH)_2$ soft sediments exhibit very narrow pore size distributions, although the variance increases slightly with solids concentration. Over 92% of pores within the 35% w/w sample were measured within the 0.24–0.47 μm range. The remaining 8% of pores were found within small modes at 3.6–4.5 nm and 9.8–12.3 μm, although it is noted LFNMR can occasionally underestimate the volume of mesoscale pores (<50 nm) due to the large echo-spacing.[27] Nonetheless, the soft sediment microstructure is dominated by

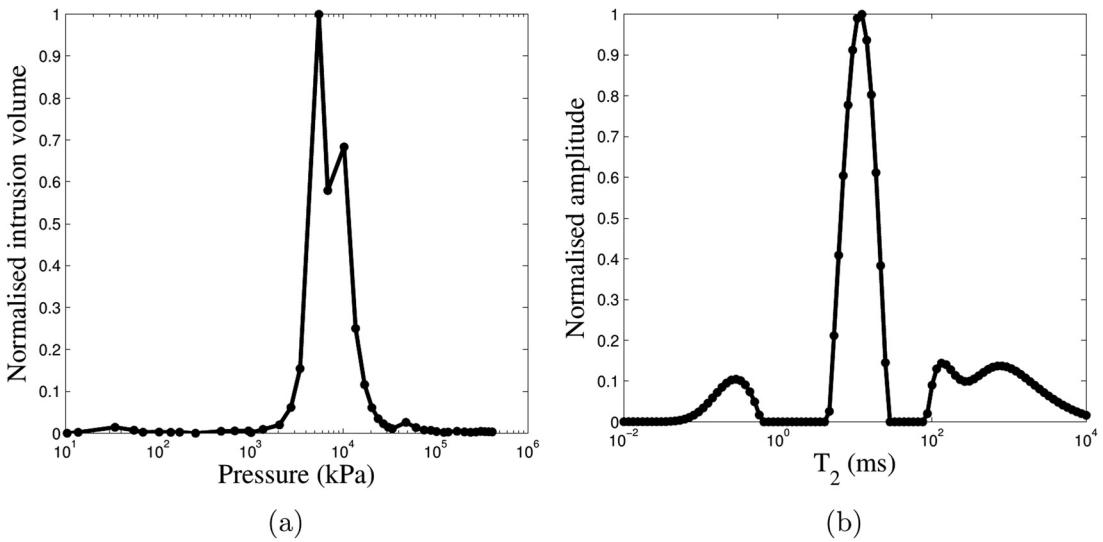

Figure 2. (a) Mercury intrusion porosimetry and (b) low-field nuclear magnetic resonance spectrograms for dried $Mg(OH)_2$ soft sediments.

Table 2. Summary of Modal Pore Throat Radii, $\bar{r}_{th}$, and Free Water Content Within $Mg(OH)_2$ Soft Sediments Estimated Using LFNMR

Test material	ω (kg/kg)	Water content (kg/kg) Total	Water content (kg/kg) LFNMR	$\bar{r}_{th}$ (μm)
$Mg(OH)_2$ (dried and saturated)		0.36	0.36	0.087
$Mg(OH)_2$	0.54	0.46	0.40	0.148
$Mg(OH)_2$	0.45	0.55	0.49	0.210
$Mg(OH)_2$	0.35	0.65	0.60	0.335

macro-pores (>50 nm)[27,28] with pore throats an order of magnitude smaller than the laser scattering derived median particle size of around 4 μm.[26]

The modal pore throat radii are summarized in Table 2, along with the LFNMR estimated mass fraction of free water detected in each sample. For the dried and re-saturated sample, the LFNMR estimated free water content corresponds closely to the increase in mass following saturation. Conversely, for the saturated soft sediment samples around 9–13% of the total water content was not detected by the LFNMR, which could indicate that some of the pore water is not *free* but immobilized within $Mg(OH)_2$ aggregates and fine meso-scale pores, or bound to the pore walls.

In backscattering detection mode, the cryo-FIB image in Figure 4a shows a large volume of dark pores in the order of 1.5–2.3 μm wide and occasionally up to 6 μm long. Interpolating between the LFNMR analysis at 35 and 45% w/w in Table 2, the modal pore throat radius at 40% w/w solids concentration is anticipated to be in the order of 0.3 μm. Assuming these throats correspond to the 1.5–2.3 μm wide pores in Figure 4a, this implies a pore body to throat ratio in the order of 5–8. While the pores appear discrete from the sublimed topography in Figure 4a, the FIB cross-section in Figure 4b demonstrates the continuous nature of the water-filled pores more clearly.

Three mechanisms of bubble growth within soft sediments are frequently discussed; excess bubble pressures required to: (1) invade adjacent pore-space, ΔP_i,[60] (2) elastically expand the host pore, ΔP_e,[4,61] and (3) propagate an existing fracture, ΔP_f,[1] are characterized in Eq. 14

$$\Delta P_i = P_b - P_w = \frac{2\gamma\cos(\theta)}{r\text{th}}$$
$$\Delta P_e = P_b - \sigma = \frac{4}{3}\tau\left(1 - \ln\left|\frac{G}{\tau}\right|\right) \quad (14)$$
$$\Delta P_f = P_b - \sigma \approx 1.32\left(\frac{K_{Ic}^6}{V_c E}\right)^{\frac{1}{5}}$$

where γ is the surface tension, G is the shear modulus, $K_{I,c}$ is the fracture toughness, V_c is a crack volume, and E is the Young's modulus of the sediment; the excess bubble pressure for cavity expansion and fracturing are given by the difference between internal bubble pressure, P_b, and the bulk sediment stress, σ, whereas the internal pressure for capillary invasion is determined by the difference between the internal bubble and local pore water pressure, P_w.[62] The pore-scales indicated by Table 2 and Figure 4 appear to preclude capillary invasion as a realistic mode of bubble growth. A non-wetting gas ($\cos(\theta) \to 1$) intruding into a 200 nm diameter pore would entail capillary entry pressures of 1.46 MPa, over three orders of magnitude larger than the shear yield stress of any sample in this study. Bubble growth beyond the pore scale must therefore require some displacement of the sediment matrix. Since the yield stress of the sediment matrix increases much more rapidly than pore dimensions constrict with sediment consolidation, capillary invasion thereby becomes more energetically favorable with sediment consolidation, but remains unrealistic even for kiloPascal yield stress $Mg(OH)_2$ sediments. Furthermore, the fracture toughness of a soft sediment is reported to scale with the inverse square root of the grain size, r_g,[63] implying that very fine-grained sediments such as this are more likely to promote fracture than dendritic bubbles consistent with capillary invasion. However, since fracture toughness typically increases with diminishing yield stress,[17] broadly spherical bubbles consistent with elastic cavity expansion are anticipated for fine-grained, low-intermediate yield stress sediments, although fracture propagation may be realistic for kiloPascal yield stress sediments containing sufficiently large initial cracks.

X-ray computed tomography

Figure 5 shows typical x-ray CT slices through $Mg(OH)_2$ soft sediments of 30, 234, and 1112 Pa yield stress following 6 h *in situ* gas generation. In each instance, a small number of

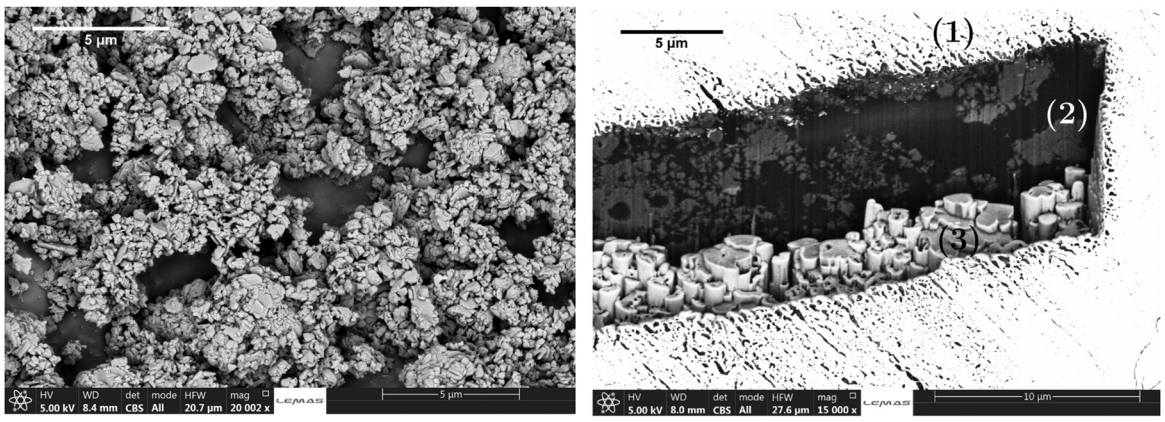

(a) (b)

Figure 4. Focused ion beam micrograph of (a) a fractured surface and (b) a FIB cross-section of cryogenically frozen $Mg(OH)_2$ soft sediment showing (1) the sediment surface, (2) a vertical cross-section with darker regions representing water filled pores, and (3) the floor of the FIB-etched borehole.

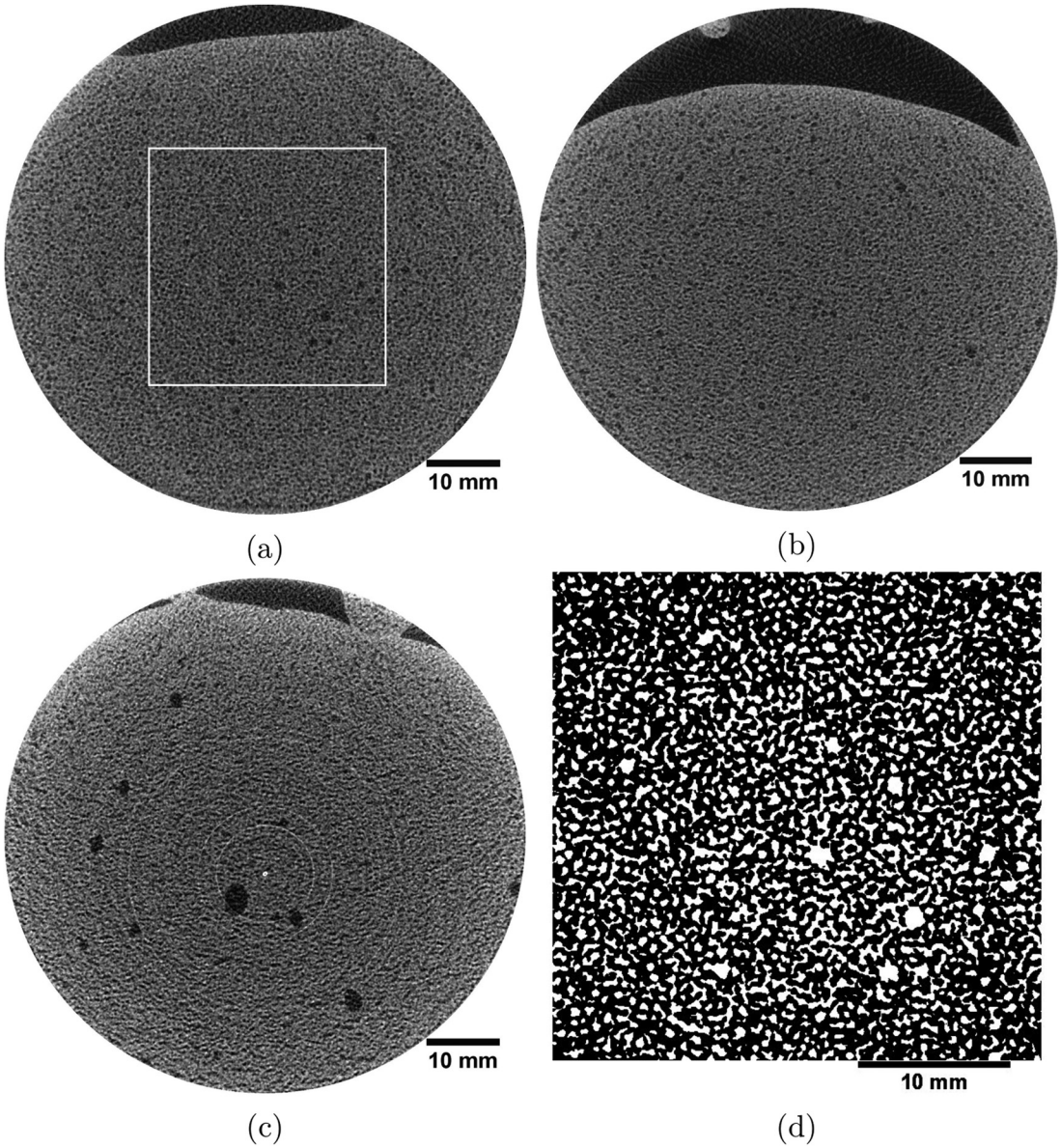

Figure 5. Example x-ray tomographs through the cylindrical cross-section of three $Mg(OH)_2$ soft sediments of (a) 30 Pa, (b) 234 Pa, and (c) 1112 Pa yield stress following 6 h *in situ* gas generation; the 600 × 600 pixel region of interest outlined in (a) has been processed and thresholded in (d) to show white bubbles against black sediment.

relatively large (>1 mm) macro-bubbles of high sphericity are observed, consistent with those identified within the same test material at larger scale and reduced resolution in Johnson et al.[11] The 1112 Pa sediment imaged in Figure 5c retains larger macro-bubbles than the two lower strength sediments, up to 10 mm in diameter. In each sediment, the vast bulk of the voidage consists of a *honeycomb* of smaller bubbles in the 0.07–0.7 mm diameter range, henceforth referred to as microvoids, many of which appear to be connected. The small bubble population within the high strength 1112 Pa sediment appears more like micro-cracks, orientated laterally, or normal to the compressive load, with significantly greater aspect ratios than the highly spherical microvoids within the 30 Pa sediment.

While 0.07–0.7 mm microvoids are indeed small relative to the macro-bubbles several millimeters in diameter, they remain 2–3 orders of magnitude larger than the undisturbed sedimentary pores observed in Figure 4. As such, the microvoids appear to straddle two classic classifications of sedimentary bubbles[2,64]: type III sediment displacing bubbles which expand the interstitial pores in the sediment and type II *reservoir* bubbles which occupy multiple pores around undisturbed sediment grains. Instead, the tomography appears to demonstrate microvoids which expand their host cavity causing the pore throats to widen in unison with the pore bodies. Eventually, the pore throats widen sufficiently for gas to intrude, allowing neighboring microvoids to coalesce and form extensive networks. This also implies that the pore geometry and deformability of these low-intermediate strength sediments is not conducive to *snap off*,[65] whereby gas invading into adjacent porespace divides at constricted throats and forms separate smaller bubbles.

Microvoid coalescence is a familiar concept to metallurgists as it represents a critical component of fracture propagation[66]

Table 3. Characterization of the Voidage Within 30–1112% w/w $Mg(OH)_2$ Soft Sediments Following 6 h *In Situ* Gas Generation

τ (Pa)	ν	$\frac{V_g^*}{V_g}$	$\frac{6V_g}{A_g}$ (mm)	$\frac{A_g}{A_s}$	$\overline{AR}^{-1}(\overline{L}_b < 0.5\,\text{mm})$	$\overline{L}_{50}$ (mm)	$\overline{L}_{95}$ (mm)
30	0.31	0.998	0.34	324	0.69	0.47	1.33
234	0.28	0.981	0.34	293	0.53	0.42	1.31
1112	0.34	1.000	0.43	281	0.51	0.50	2.70

and failure within ductile metals.[67] Coalescence between microvoids within aqueous soft sediments may play a similar role in diminishing the fracture toughness of the bulk sediment, however another implication could be that extensive networking of coalesced microvoids establishes pathways for enhanced gas migration and chronic gas release. The connectivity among the microvoid population is clearest in Figure 5d, where the region of interest outlined in white in Figure 5a has been isolated, magnified and processed to diminish speckling and ring artefacts (shown most clearly in Figure 5c), thresholded and inverted to present white bubbles against a dark soft sediment background. A number of characteristics of the bubble population are summarized in Table 3.

The thresholded void fractions of the 600^3 voxel regions of interest lie within the 0.28–0.34 range, which aligns closely to the void fractions of 0.30–0.38 estimated from the increase in bed volume, obtained by approximating the bed as a partially filled cylinder with a domed surface.[11] Thus, essentially the entire bubble population appears to be observable at this 53.25 μm imaging resolution. A crude characteristic dimension of the bubble population can be obtained from the total retained gas volume to surface area ratio, $\frac{6V_g}{A_g}$. This characteristic bubble length ranges from 0.34 to 0.43 mm for the three sediments, comfortably larger than the CT imaging resolution in this study, however it also indicates why only the very mature bubbles are observable under large scale clinical CT[11] with slice separations in the order of 0.625–1.25 mm, as summarized in Table 1. The fact that this characteristic length-scale of the retained bubbles is two orders of magnitude smaller than the 32 mm wide region of interest also indicates that the cubic sub-sample is representative, justifying its use for the more computationally intensive post-processing steps.

The total interconnected bubble volume was determined by counting the number of face, edge and corner connected bubble voxels using the Bolte and Cordelières[41] algorithm, revealing that the volume of the continuous gas networks, V_g^*, account for at least 98.1% of the total free gas volume, V_g, within the 31.95 mm wide region of interest, as detailed in Table 3. The bubble network therefore provides a pathway for free gas to migrate through the region of interest by diffusion. Competition between the maximum field of view and the imaging resolution necessary to capture the entire bubble population makes it difficult to estimate the range that the bubble network might span. The field of view could be representative of the sediment on an infinite scale, making 98% of the retained free gas continuous. Alternatively, the gas could be retained within discontinuous *ganglia*[9] which could span length-scales as little as 0.1 m, barely larger than the 31.95 mm wide field of view, similar to observations of two-phase N_2-brine flow through porous sandstone[68] and dense non-aqueous fluid contamination in soils.[69] In either instance, the extensive connectivity between neighboring bubbles is likely to have significant implications for gas migration and chronic gas release.

Diffusion through permeable bubble networks would explain chronic gas release from soft sediments much better than aqueous volatile diffusion as gas molecules diffuse much more readily in the gas phase than through an aqueous phase. The self-diffusion coefficient for oxygen, 1.92×10^{-5} m^2 s^{-1},[58] is four orders of magnitude greater than that of oxygen in water, 3.49×10^{-9} m^2 s^{-1}.[70] Furthermore, the ratio of free gas surface area within the bed to the surface area of the interface between the bed and the test cylinder ullage, $\frac{A_g}{A_s}$, indicates there is around 300 times more interfacial area for exchange of volatiles within the bed than at the bed-ullage boundary, and this factor is likely to increase substantially with experimental scale. Hence, conditions are many times more favorable for the release of free gas than for direct release of dissolved oxygen from the aqueous phase, consistent with observations from marine sediments.[7] Gas diffusion through permeable bubble networks also reconciles chronic gas release with the observation that the large macro-bubbles which impart the greatest buoyant stress on the sediment and are most likely to rise by ebullition appear to remain static within the bed for several hours.[11]

In order to better visualize the constituent bubbles of each network, a 2–3 voxel deep film was digitally eroded from the void-space to reduce the connectivity between adjacent bubbles and reveal discrete bubbles, generating the views in Figures 6a–c. These depictions thereby under-represent the volumetric contribution of the microvoid population to the total voidage, but better demonstrate the size and shape of retained bubbles under the different sediment conditions. The microvoid population is more distorted within the higher concentration sediments, with the average inverse aspect ratios, $AR^{-1} = \frac{L_{\min}}{L_{\max}}$ decreasing significantly, from 0.69 in the 30 Pa sediment to 0.51 at 1112 Pa yield stress. The longest axes of these fine bubbles are typically orientated normal to the compressive load, particularly within the 1112 Pa sediment, indicating that young bubbles grow by preferentially displacing sediment in the direction of minimum compressive stress. The increasing aspect ratio with sediment consolidation thereby accords with the observation that the ratio of lateral to vertical compressive stress, $K_0 = \frac{\sigma_H}{\sigma_V}$, decreases with increased sediment depth and with consolidation.[71] Preferential bubble deformation in the lateral direction also promotes coalescence in the radial field, instigating a least tortuous diffusion path perpendicular to gravity.

Estimation of bubble aspect ratios as a function of bubble size enabled translation[44,45] of 3×10^8 random chord length measurements of the void-space into the BSD presented in Figure 6d. Bubbles of 0.07–10 mm characteristic length are observed in each instance, with remarkably similar median sizes of 0.42–0.50 mm, summarized in Table 3. These sub-millimeter median bubble diameters appear comparatively small compared with previous observations of sedimentary bubbles. Sherwood and Eduardo Saacute;ez[14] observed bubbles of 3 mm median diameter following hydrogen peroxide decomposition in low strength ($\tau =$ 7 Pa) bentonite clay, used as an analogue for nuclear waste slurries stored at Hanford, although the lower limit of detection in this study was unclear. As demonstrated by Figure 6c, the 1112 Pa yield stress sample

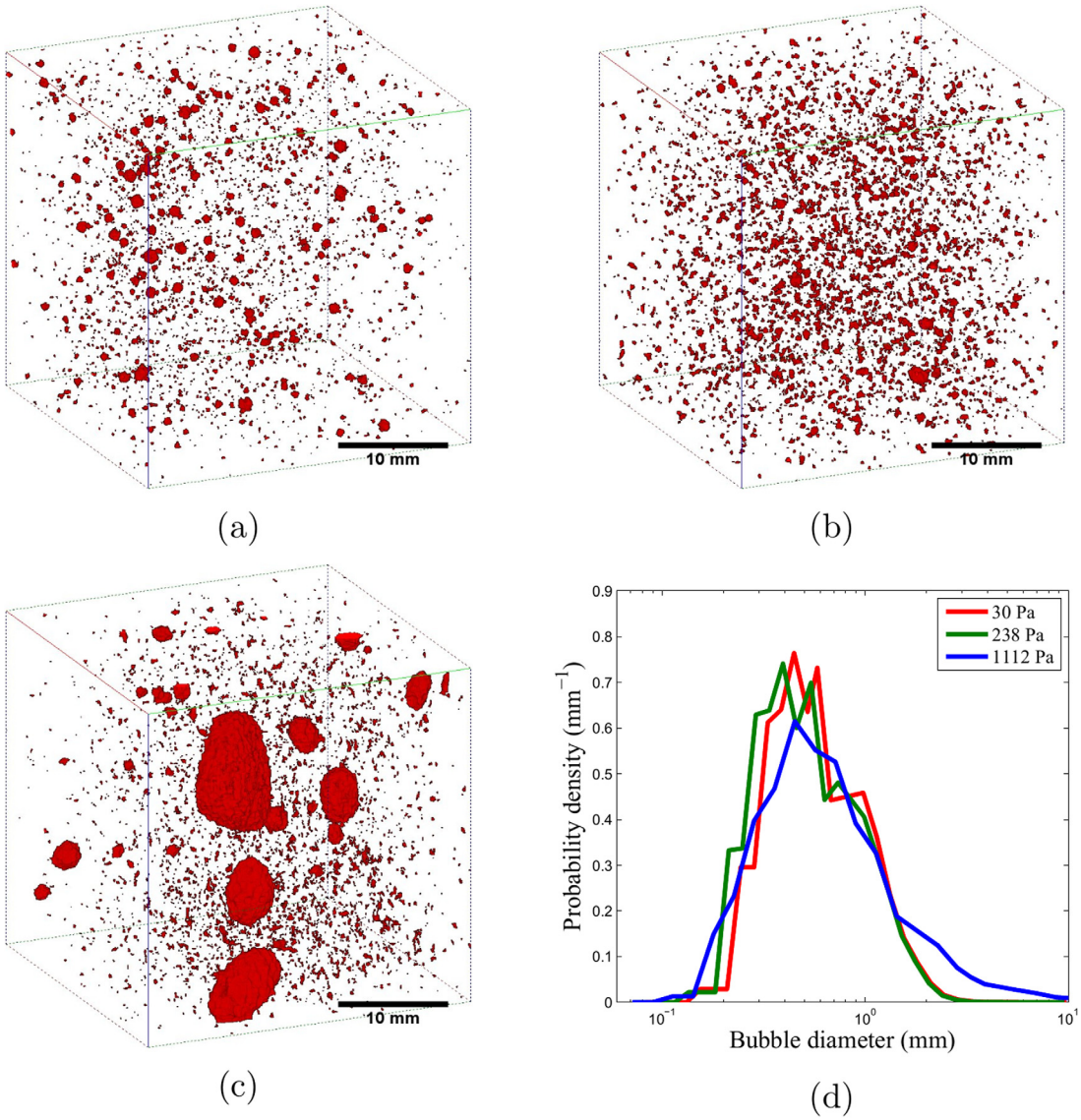

Figure 6. Three-dimensional views of *partially eroded* bubble networks indicating the size and shape of individual bubbles within (a) 30, (b) 234, and (c) 1112 Pa soft sediments together with (d) bubble size distribution histograms from chord length analysis.

[Color figure can be viewed at wileyonlinelibrary.com]

supports a larger fraction of macro-bubbles, with 10.9% of the voidage consisting of large mature bubbles of $1.5 < \overline{L} = L_{max}\sqrt{AR} < 10$ mm dimensions, while less than 3% of bubbles within the less consolidated samples exceed 1.5 mm in length. Integration of this large bubble fraction within the much larger void-network may account for their long residence times and why bubbles cease to grow despite continued *in situ* gas generation,[11] since volatiles which diffuse toward networked bubbles may permeate or diffuse through the network rather than promote further growth. LBM and Monte Carlo simulations are employed to characterize gas migration through these sedimentary void-networks.

Characterizing the permeability of bubble networks with LBM

Lateral gas flow through the coalesced bubble networks within the 30 Pa yield stress soft sediment was investigated by running an LBM simulation for 70,000 computational iterations, equivalent to 1.62 s, at which point the superficial velocity was observed to achieve steady state; an example two-dimensional velocity field, in the x–y plane, at steady state is shown in Figure 7a. Positive velocities in the x-direction, u_x, were observed in 89.9% of fluid sites, demonstrating continuous flow of gas through the sampled volume. The high velocity regions, indicated by warmer colors, demonstrate preferential flow pathways through the sediment.

The evolution in superficial velocity, or Darcy velocity, through a plane at the mid-point of the volume (x = 200 voxel) is presented for flow through the three soft sediments in Figure 7b until steady state conditions were observed. The six profiles represent flow in the lateral, u_x, (solid lines) and vertical, u_y, (dashed lines) directions through the 30, 234, and 1112 Pa yield stress sediments. The principal flow direction for lateral and vertical simulations was specified by both the direction of the imposed pressure gradient and the provision of a solid duct around the sample with walls normal to the pressure gradient. From Darcy's law, Eq. 8, it is shown

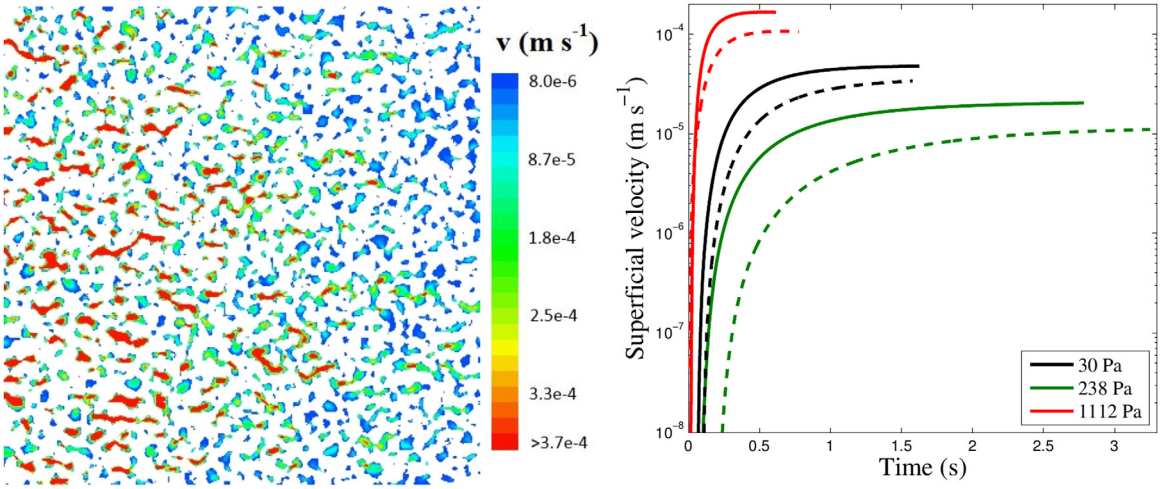

Figure 7. LBM simulations of flow through sedimentary void-networks given a 1.65 Pa m^{-1} lateral pressure gradient, including (a) an example velocity field in the x–y plane through the bubble networks of a 30 Pa yield stress soft sediment, white pixels represent regions of zero flow, including the bulk sediment (solids and pore-water) sites and bubbles not connected to the continuous void-network, velocities through the void network are represented using a blue–red color map with velocity increasing with the color warmth, and (b) the evolution in superficial velocity at the mid-point of the porous volume in the lateral (solid line) and vertical (dashed line) directions.

[Color figure can be viewed at wileyonlinelibrary.com]

that for a given pressure gradient, and fixed viscosity and density of fluid, in this case oxygen, the permeability of the void-space depends only on the superficial velocity, enabling calculation of the lateral, k_H, and vertical, k_V, permeabilities as summarized in Table 4.

In each instance, the voidage is 39–46% less permeable to vertical flow than to horizontal, or lateral, flow ($\kappa_H > \kappa_V$). Since the LBM simulations were performed in a zero-gravity environment, the enhanced permeability to lateral flow must be a consequence of the geometry of the void-network, specifically the tortuosity and constrictivity of the pathways, as the three sediments exhibit similar gas holdup with high bubble connectivity, encompassing >98% of the total void fraction. Following Figure 6 it was noted that the microvoids are deformed by the sediment with their longest axis oriented perpendicular to the compressive load, or parallel to the minimum compressive stress. Since the deformed bubbles occupy more space normal to gravity, bubbles are more likely to encounter, and coalesce with, neighboring bubbles in the radial field. This explains the propagation of a less tortuous pathway normal to gravity promoting lateral gas migration.

The LBM simulated permeabilities exhibit the same hierarchy ($\kappa(\tau = 1112\,\text{Pa}) > \kappa(\tau = 30\,\text{Pa}) > \kappa(\tau = 234\,\text{Pa})$) as the void fractions summarized in Table 4, with sediments of greatest gas holdup most pervious to gas migration. For geometrically similar microstructures, Quispe et al.[51] discusses a power law relationship between permeability and porosity, or void fraction in this instance, with a cubic exponent. The subtle difference in gas holdup between samples does not therefore account for the range of permeabilities observed, implying that geometric differences between the void-networks significantly influence the gas transport behavior. Following Figure 3, consolidation of the sediment to higher solids concentrations and yield stresses has been shown to constrict the throats connecting pores within the two-phase sediment microstructure. This may manifest in greater constrictivity between the partially coalesced microvoids as the yield stress is increased from 30 to 234 Pa, explaining the reduction in permeability. The reason this trend does not continue to the 1112 Pa sediment is most likely due to the onset of fracture,[11] particularly among the small bubble population, and the merging of these lateral micro-cracks to establish low-tortuosity pathways.

However, the hierarchy of the permeability coefficients may be less significant than their magnitude, which lie in the order of 10.1–151.6 $\times$ 10^{-12} m^2, as summarized in Table 4. Permeability coefficients of this magnitude are consistent with highly pervious geological media[72]; this is perhaps unsurprising given that the 0.07–10 mm bubbles comprising the void-network are much coarser than typical geological pores. The high magnitude permeabilities imply that gas will readily migrate through these sediments once a long range void-network is established.

The pressure field within soft sediments is said to increase linearly with depth,[6] a phenomenon which sometimes causes large bubbles to acquire an inverted teardrop shape as the change in pressure across the height of the bubble can lead to

Table 4. The Gas Permeabilities of Bubble Networks Retained Within Mg(OH)$_2$ Soft Sediments of 30–1112 Pa Yield Stress

ω (%w/w)	τ (Pa)	ν	κ_H ($\times 10^{-12}$ m^2)	κ_V ($\times 10^{-12}$ m^2)	κ_V/κ_H
35	30	0.31	50.2	30.9	0.61
45	234	0.28	18.6	10.1	0.54
54	1112	0.34	151.6	91.8	0.61

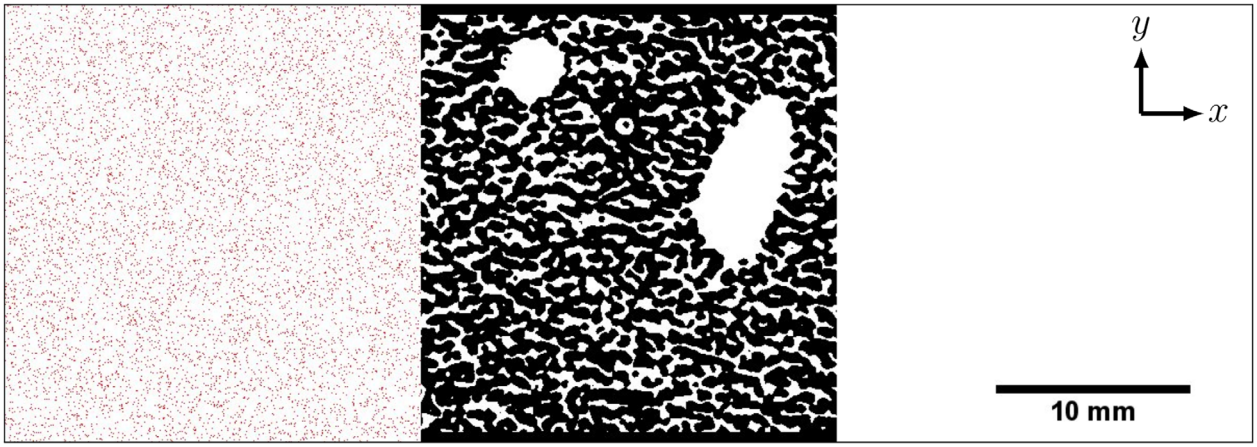

Figure 8. An example two-dimensional slice (normal to the z-direction) through the constructed domain for the Monte Carlo gas diffusion simulations at the initial condition; the three regions from left to right represent the source, porous medium and sink regions, where the porous medium is generated from a CT reconstruction of the 1112 Pa sample with the voidage thresholded white.

[Color figure can be viewed at wileyonlinelibrary.com]

a reduced load at the *tail* causing it to narrow. The increase in pore water pressure with depth will be less than the increase in hydrostatic pressure, $\Delta P = \rho g L$, as the large compressible bubbles transfer a portion of the load to the solid sediment matrix.[2] Sediments with substantial gas holdup or even continuous gas may greatly dampen the hydrostatic load. Nonetheless, given the large permeabilities to vertical flow in the order of 10–90 $\times$ 10^{-12} m^2, a mild increase in the ambient pressure field surrounding the bubble network with depth may provide adequate driving force for volatiles to permeate upwards toward the shallow surface of the bed according to Darcy's law, Eq. 15, a process we will call *stratification.*

$$q = \frac{\dot{V}}{A} = \frac{\kappa_V}{\mu_g}\frac{\Delta P}{L} \tag{15}$$

However, the vertical pressure gradient may be greatly dampened by the large holdup of cavity expanding bubbles and the orientation of individual microvoids and cracks promotes gas migration normal to the compressive load. Long range gas migration may instead be controlled by lateral diffusion, driven by concentration gradients resulting from the continuous *in situ* generation of volatiles, enabling chronic gas release at containment walls. Analysis of lateral diffusion of volatile species through the void-network requires characterization of the effective diffusivity, which is investigated by Monte Carlo simulation.

Characterizing effective diffusivity through permeable bubble networks by Monte Carlo simulation

Figure 8 shows a slice through the thresholded 1112 Pa sediment between a source region (left) populated with red tracer particles and an empty sink region (right) prior to commencement of diffusion. Tracer concentration profiles during a Monte Carlo diffusion simulation through an empty duct are presented at 1 $\times$ 10^5 step intervals in Figure 9a. The three regions demarcated by vertical dashed lines represent the source, duct and sink regions from left to right. The blue profile, after 1 $\times$ 10^3 computational steps closely resembles the square-step initial condition, indicating minimal diffusion during this time-scale. Subsequent profiles demonstrate the anticipated bell-shaped Gaussian concentration profiles. As the source and sink regions share the same diffusivity as the open duct, a continuous Gaussian distribution extends across the entire 1200 voxel domain, resulting in the concentration at the entry to the duct, $\phi(h,t)$, evolving significantly with time. The reflection and superposition of particles at the end of the sink region, $x = L$, sees the minimum concentration plateau at increasing concentrations, up to 92 molecule mm^{-3} at the 5 $\times$ 10^5 step.

The thick dashed lines represent analytical solutions obtained using Eq. 11 with a diffusivity of 4.15 $\times$ 10^{-4} mm^2 $step^{-1}$, demonstrating excellent agreement with the simulated profiles throughout the 5 $\times$ 10^5 step period, particularly during the first 4 $\times$ 10^5 iterations. The final analytical profile marginally over-predicts the simulated tracer concentration, possibly indicating a slight concentration dependency in the diffusion coefficient, however the small disagreement between the model and the latter stages of the simulation fell within an acceptable tolerance. Oxygen tracers diffuse through oxygen with a self-diffusion coefficient of 19.2 mm^2 s^{-1};[58] comparison of the virtual and physical diffusion coefficients calibrates the duration of a computational iteration, Δt, which was found to be 2.16 $\times$ 10^{-5} s. Each computational time step is therefore five orders of magnitude larger than the collision period for oxygen molecules of 149 $\times$ 10^{-12} s,[73] and so a tracer will undergo roughly 1.45 $\times$ 10^5 intermolecular collisions at each iteration of the simulation. Given that a tracer can travel up to $\sqrt{3}$ voxel, or 92 μm, during a computational iteration, intermolecular collisions outweigh wall-collisions many-fold, and so tracer migration is governed by bulk, rather than Knudsen, diffusion.

Tracer concentration profiles through the voidage of the 1112 Pa $Mg(OH)_2$ soft sediment are presented in Figure 9b. As for the empty duct, six profiles are shown at regular intervals for the first 5 $\times$ 10^5 step, or 10.8 s, of diffusion. The concentration profiles through the sediment demonstrate the same Gaussian tail shape as through the empty duct, however there is a sudden drop in tracer concentration over the last 50 voxel, or 2.7 mm, of the bed due to the sudden expansion at $x = 2h$. Since the objective is to ascertain the diffusivity through the porous sediment only, the problem can be reformulated to consider only the x = 400–750 voxel, or 21.3–39.9 mm, region during the first 5 $\times$ 10^5 step. A simpler

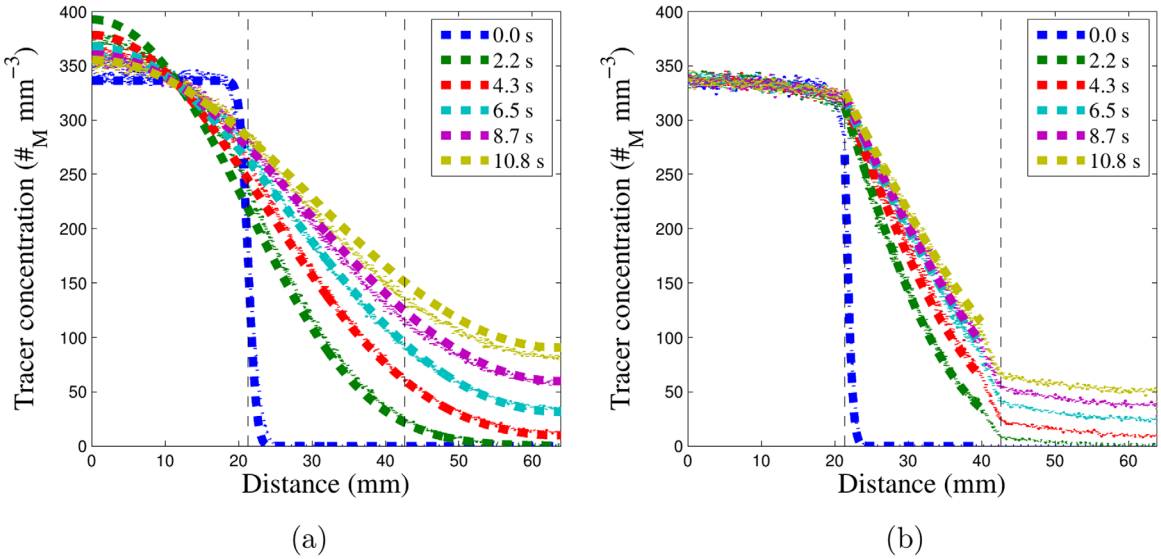

Figure 9. Evolution of oxygen tracer concentration in time and space, $\phi(x,t)$, during Monte Carlo gas diffusion simulations within (a) an open duct and (b) the permeable void networks within 1112 Pa yield stress $Mg(OH)_2$ soft sediment (see Figure 8); the dotted line profiles are obtained from the simulations, $\phi(x,t)$, the thick dashed lines represent optimized analytical solutions, $\hat{\phi}(x,t)$, and the vertical dashed lines demarcate the source, porous and sink regions.

[Color figure can be viewed at wileyonlinelibrary.com]

analytical solution can therefore be found by assuming a planar source concentration at $x = h$ obtained from the simulation, $\hat{\phi}(h,t)$, and by neglecting the reflection of particles at $x = L$, which is not relevant during the early iterations of the simulation, where the diffusion length, $L_D = 2\sqrt{Dt}$, is less than 1200 voxel, or 63.9 mm. This solution is given in Eq. 16 and the divergence between the simulated and analytical concentration profiles, E, is determined for the truncated, 400–750 voxel, area of interest.

$$\phi(x,t) = \hat{\phi}(h,t)\,\mathrm{erfc}\left(\frac{x-h}{2\sqrt{Dt}}\right) \text{ for } x > h \tag{16}$$

$$D = D_{eff} \text{ when } E \rightarrow \text{minimum where :}$$

$$E = \sum_{t=1\times10^3\,\text{step}}^{5\times10^5} \sum_{x=400\,\text{voxel}}^{750} |\hat{\phi}(x,t) - \phi(x,t)|$$

The effective diffusion coefficients for each sediment are summarized in Figure 10. The diffusion simulations through each of the permeable bubble networks were characterized by the curious observation that diffusion slowed over time, manifesting in effective diffusion coefficients, which diminished by up to 41% during the simulation. While there is precedent for effective diffusivities through porous media to exhibit some concentration dependence,[57] the slowing of diffusion could represent an artefact of the simulation resulting from the coarseness of the voxels relative to the scale of constrictions in the void-network, or *necks* between partially coalesced bubbles. As these constrictions are typically only 1–3 voxel wide, tracer particles are sometimes forced to diffuse through in single file even though these constrictions are orders of magnitude larger than the mean free paths of oxygen or hydrogen. Hence, as the tracer concentration increases within the voidage, the resistance to diffusion artificially increases. Under these conditions, the predicted diffusivities will be most reliable at the early stages of simulation when the tracer concentration within the soft sediment is low.

The effective diffusion coefficients at each sediment concentration exhibit the same hierarchy as the permeability coefficients, whereby $D_{\text{eff}}(\tau = 1112\,\text{Pa}) > D_{\text{eff}}(\tau = 30\,\text{Pa}) > D_{\text{eff}}(\tau = 234\,\text{Pa})$, although the effective diffusivities lie within a narrower range of 0.4–1.5 × 10^{-5} m^2 s^{-1}. Equally, the 1112 Pa sediment demonstrates that diffusive transport proceeds preferentially normal to gravitational compression. This reinforces the arguments made that (1) gas migrates efficiently through high strength sediments with shear yield stresses in the order of a kiloPascal due to the merging of microcracks, (2) at yield stresses below the fracturing regime sediment consolidation increases the constrictivity of throats between coalesced microvoids and increases the

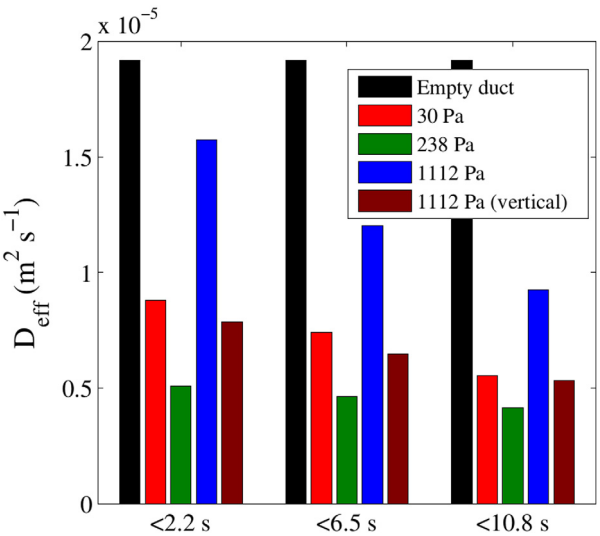

Figure 10. Summary of the effective diffusivities for oxygen tracers through an empty duct and through permeable bubble networks within 35–54% w/w $Mg(OH)_2$ soft sediments.

[Color figure can be viewed at wileyonlinelibrary.com]

tortuosity of the diffusion path, and (3) microvoids deform with their longest axis favoring the direction of minimum compressive stress, normal to gravity, promoting the formation of lateral rather than vertical transport pathways.

The question remains as to what effective diffusivities in the order of 0.5–1.5 × 10^{-5} m^2 s^{-1} signify for gas migration on the timescales that gas is generated within marine and nuclear sediments. Methanogenic gas generation rates within marine sediments span five orders of magnitude from 1 μmol m^{-3} d^{-1} to 100 mmol m^{-3} d^{-1}.[74] Sludge waste within underground tanks at Hanford generates hydrogen, methane and nitrous oxide at rates in the order of 1 mmol m^{-3} d^{-1},[14] while the hydrogen generation rates within CMS at Sellafield are anticipated to be marginally higher due to the presence of uncorroded metallic cladding swarf. As such, gas generation can be considered a chronic process; even at the fastest gas generation rates in the order of 100 mmol m^{-3} d^{-1} a cubic meter of sediment would require 41 d to generate sufficient volatiles to occupy 0.1 m^3 at ambient temperature and pressure. Within the same time frame, gas can migrate through a continuous void-network with a diffusivity of 1 × 10^{-5} m^2 s^{-1} up to a diffusion length of 11.9 m, comfortably sufficient to diffuse to the walls of nuclear legacy waste containers and facilitate methane release from shallow marine sediments where gas retention is typically greatest as the rich organic content fuels enhanced methanogenesis.[20]

Alternatively, the characteristic time for a one-directional concentration gradient across a given distance, x, to diminish by half, $t_{1/2}$, as a result of diffusion through the void-space can be determined from Eq. 17

$$\operatorname{erf}\left(\frac{x}{2\sqrt{D_{\text{eff}}t_{1/2}}}\right)=0.5 \qquad \therefore t_{1/2}=1.099\frac{x^2}{D_{\text{eff}}} \tag{17}$$

Therefore, a diffusivity of 1 × 10^{-5} m^2 s^{-1} will result in a concentration gradient diminishing by half in 5 d across a 2 m distance, or 32 d across a 5 m distance. Within the same 32 d period no more than 3.2 mol gas is generated per cubic meter of sediment. Hence, diffusion through the void-network appears to be rapid in comparison to the rate of gas generation, implying that the sediment is unlikely to continue to swell once a continuous void-network is established. Furthermore, gas diffusion would proceed even faster if *in situ* hydrogen were generated rather than oxygen, since it has a self-diffusion coefficient of 1.604 × 10^{-4} m^2 s^{-1},[59] a factor of 8.3 larger than that of oxygen. However, based on x-ray tomography analysis within a 32 mm field of view it cannot necessarily be assumed that the gas phase is continuous over several meters. It is possible that the gas is retained within discontinuous *ganglia* which could span little more than the CT field of view. The latter possibility draws parallels to synchrotron x-ray tomography observations of two-phase N_2 − brine flow through porous sandstone,[68] and dense non-aqueous fluid contamination in soils.[69]

In the eventuality that the gas phase is not continuous at the meter-scale, three mechanisms could contribute to gas migration over longer distances. Ambient pressure fluctuations which cause the free gas to advance and recede[13] could promote: (1) dynamic connectivity between neighboring ganglia which is not visible during an instantaneous scan,[68] or (2) ganglion migration through the sediment via Haines jumps,[75] whereby gas intruding through a pore throat passes into the adjacent pore body manifesting in a sudden drop in capillary pressure, bubble expansion, and a rapid transfer of elastic potential energy to kinetic energy.[75,76] Berg et al.[75] employed synchrotron x-ray tomography to reveal that Haines jumps can promote gas migration over scales of around 20 individual pore lengths, which, given the distribution of free gas in Figure 5, may in turn promote further partial coalescence events. Bubble transport by Haines jumps is consistent with a recent study by Liu et al.[77] which demonstrated that gas release from sediments, subject to a sudden reduction in hydrostatic head, is driven by the mobility of the smallest bubbles along macropores. Partial bubble coalescence across multiple pore bodies represents a realistic mechanism for establishing macropores, orders of magnitude larger than the interstitial pores observed prior to gas generation.

In addition, the large 28–34% holdup of ≈0.4 mm median diameter bubbles provides a large interfacial surface area for continuous exchange of volatiles between the free gas and aqueous phases, while the distance separating bubbles which are not integrated into the continuous network are typically no more than a millimeter. Hence, long range gas migration and chronic release could be explained by (3) a composite mechanism of fast diffusion through highly permeable void-networks, gas exchange at the interface and short range aqueous diffusion. All three processes are likely to operate in tandem to contribute toward an enhanced rate of volatile transport in comparison to aqueous diffusion alone.

The least efficient possible route for gas migration considers only the latter possibility of composite diffusion through static ganglia, 0.1 m in length, and aqueous diffusion across 1 mm distances of intermediate soft sediment. Since aqueous diffusivities are around four orders of magnitude lower than the self-diffusivities of oxygen and hydrogen, gas migration across a 2 m distance would be limited by diffusion through the 20 mm of sedimentary water rather than the 1.98 m of diffusion through the gas phase. Using a conservative assumption that the aqueous diffusivity of oxygen of 3.49 × 10^{-9} m^2 s^{-1} is diminished by an order of magnitude to correct for the tortuosity of the diffusion path,[70] gas can diffuse across 20 mm of sediment within 3.3 d, around treble the 1.1 d period required to migrate across a 1.98 m diffusion length through the gas phase. The composite diffusion time of 4.4 d can still be considered rapid in comparison to timescales discussed for chronic gas generation by corrosion, radiolysis and methanogenesis within consolidated soft sediments.[14]

Thus, whether the networks of partially coalesced microvoids exist as a continuous vessel-spanning phase or discrete ganglia less than a meter in range, gaseous diffusion appears to present a viable mechanism for chronic gas release from low-intermediate strength sediments able to resist bubble ebullition but unable to support deep drainage channels. The potential for this to represent a widespread mechanism for gas migration across a broad range of sediment yield stress conditions is demonstrated by the schematic in Figure 11. The observation that 8 mm bubbles were unable to fluidize $Mg(OH)_2$ sediments of as little as 7 Pa yield stress in Johnson et al.[11] suggests that the lower bound stress at which bubble networks become the principal mechanism for gas migration, under quiescent conditions, could be as low as just a few Pascals. Conversely, the upper bound stress at which stable drainage channels are supported to depths of meters lies in the kiloPascal range.[4] It therefore appears that the limiting condition for bed swell within 10–1000 Pa yield stress

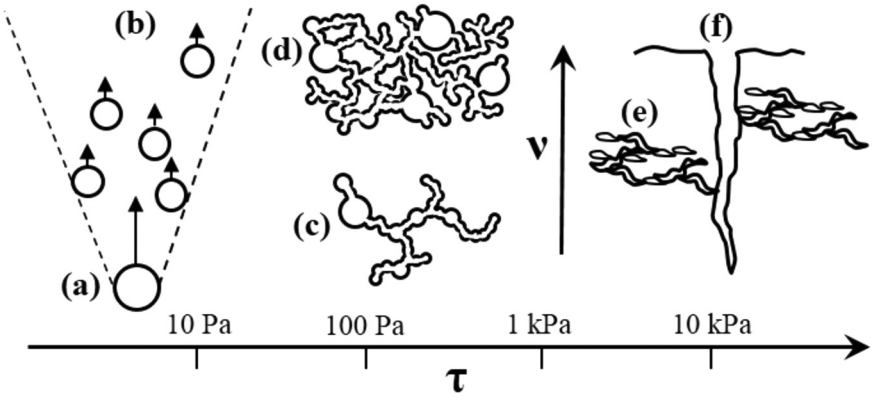

Figure 11. Schematic demonstrating alternative chronic gas release mechanisms from consolidated soft sediments under various yield stress and gas holdup conditions, including: (a) buoyant bubble ebullition, possibly inducing (b) bubble cascades,[14,78] gas migration through (c) discrete ganglia of partially coalesced bubbles or (d) vessel-spanning continuous bubble networks at higher voidages, (e) permeable pathways through coalesced micro-cracks and (f) deep vertical drainage channels.[4]

intermediate strength sediments is dictated by the establishment of sufficiently large bubble networks by partial coalescence to enable a faster rate of gas migration than gas generation.

Conclusions

Magnesium hydroxide soft sediments of 35–54% w/w solids concentration, or 30–1112 Pa yield stress, exhibited significant bed swell to 28–34% gas holdup following 6 h *in situ* hydrogen peroxide decomposition. X-ray CT revealed that the voidage consisted of a population of bubbles, 0.07–10 mm in diameter, with extensive partial coalescence between the submillimeter microvoids, which resulted in bubble networks which spanned the 32 mm field of view and comprised at least 98% of the observed free gas. Lattice Boltzmann and Monte Carlo simulations indicate that these networks are highly pervious to gas, with permeabilities of $10.1–151.6 \times 10^{-12}$ m^2 and effective diffusivities for hydrogen of $3.7–12.5 \times 10^{-5}$ m^2 s^{-1}, thereby providing avenues for rapid gas migration across the length-scale of the bubble network. Consolidation of the sediments, resulting in an increase in shear yield stress to 1112 Pa and constriction of the water filled pore throats to an LFNMR derived modal size of 148 nm, promoted fracturing among the microvoid population, while the larger bubbles maintained a more spherical geometry. Coalescence between laterally orientated micro-cracks established a low-tortuosity pathway for efficient gas transport normal to gravity, with effective diffusivities in the order of 10^{-10} m^2 s^{-1}.

Competition between the maximum scan field of view and imaging resolution required to visualize the smaller microvoids means that the scale of the void-networks remains unclear. Hence, the bubble population may consist of a continuous gas phase encompassing 98% of all retained free gas, or discontinuous *ganglia* of coalesced bubbles which span lengths of several centimeters, close to the experimental scale of this study. In the latter instance, a combination of (1) dynamic connectivity between neighboring ganglia, (2) Haines jumps causing the ganglia to migrate, and (3) composite diffusion through the gas and aqueous phase can facilitate substantially enhanced gas transport in comparison to aqueous diffusion alone. As the voidage increases to the order of 20–30% and the distance separating these discrete ganglia diminishes to millimeter scale, composite diffusion through gaseous and aqueous phases appears to facilitate gas release on a shorter time-scale than the chronic rate of gas generation within marine and nuclear waste sediments. The gas transport mechanism identified herein, provides an explanation for the long-standing enigma of how gas escapes from sediments with yield strengths higher than that in which bubble rise, or ebullition, occurs ($\lesssim$10s Pa) and lower than that where bubbles burrow by propagating temporary fractures or deep vertical drainage channels are supported ($\gtrsim$ kPa).

Acknowledgments

Thanks go to the Nuclear Decommissioning Authority (NDA), Sellafield Ltd., and the Engineering and Physical Sciences Research Council (EPSRC) for funding this work through an industrial case award (Grant EP/K504440). This work is affiliated with the Decommissioning, Immobilisation and Storage Solutions for Nuclear Waste Inventories (DISTINCTIVE) consortium (Grant EP/L014041/1). We also thank Prof. Geoff Randall and Martyn Barnes of Sellafield Ltd. for their support of this research, Karine Mardon at the University of Queensland's Centre for Advanced Imaging, and Samuel Allshorn and Carlos Grattoni of the University of Leeds Wolfson Laboratory for access to their facilities and assistance with x-ray tomography and nuclear magnetic resonance data acquisition.

Literature Cited

1. Johnson BD, Boudreau BP, Gardiner BS, Maass R. Mechanical response of sediments to bubble growth. *Mar Geol.* 2002;187(3–4):347–363.
2. Wheeler SJ. A conceptual model for soils containing large gas bubbles. *Geotechnique.* 1988;38(3):389–397.
3. Keller M, Stallard RF. Methane emission by bubbling from Gatun Lake, Panama. *J Geophys Res Atmos.* 1994;99(D4):8307–8319.
4. van Kessel T,van Kesteren WGM. Gas production and transport in artificial sludge depots. *Waste Manag.* 2002;22(1):19–28.
5. Sills GC, Gonzalez R. Consolidation of naturally gassy soft soil. *Geotechnique.* 2001;51(7):629–639.
6. Algar CK, Boudreau BP, Barry MA. Initial rise of bubbles in cohesive sediments by a process of viscoelastic fracture. *J Geophys Res Solid Earth.* 2011;116(B4):B04207

7. Katsman R, Ostrovsky I, Makovsky Y. Methane bubble growth in fine-grained muddy aquatic sediment: insight from modeling. *Earth Planet Sci Lett.* 2013;377–378:336–346.
8. Chan YJ, Chong MF, Law CL, Hassell DG. A review on anaerobic-aerobic treatment of industrial and municipal wastewater. *Chem Eng J.* 2009;155(1–2):1–18.
9. Luhmann AJ, Kong XZ, Tutolo BM, Ding K, Saar MO, Seyfried WE. Permeability reduction produced by grain reorganization and accumulation of exsolved CO_2 during geologic carbon sequestration: a new CO_2 trapping mechanism. *Environ Sci Technol.* 2013;47(1):242–251.
10. Wheeler SJ. The undrained shear strength of soils containing large gas bubbles. *Géotechnique.* 1988;38(3):399–413.
11. Johnson M, Peakall J, Fairweather M, Biggs S, Harbottle D, Hunter TN. Yield stress dependency on the evolution of bubble populations generated in consolidated soft sediments. *AIChE J.* 2017;63(9): 3728–3742.
12. Ali SA, Gauglitz PA, Rossen WR. Stability of solids-coated liquid layers between bubbles. *Ind Eng Chem Res.* 2000;39(8):2742–2745.
13. Kam SI, Gauglitz PA, Rossen WR. Effective compressibility of a bubbly slurry. II. Fitting numerical results to field data and implications. *J Colloid Interface Sci.* 2001;241(1):260–268.
14. Sherwood DJ, Eduardo Sáez A. The start of ebullition in quiescent, yield-stress fluids. *Nucl Eng Des.* 2014;270:101–108.
15. Dubash N, Frigaard IA. Propagation and stopping of air bubbles in Carbopol solutions. *J Nonnewton Fluid Mech.* 2007;142(1–3): 123–134.
16. Dorgan KM, Jumars PA, Johnson B, Boudreau BP, Landis E. Burrow extension by crack propagation. *Nature.* 2005;433(7025):475
17. Mughrabi H. Plastic deformation and fracture of materials. In: Haël Mughrabi, editor. *Materials Science and Technology—A Comprehensive Treatment*, Chapter 1, Vol. 6, VCH, Weinheim, 1992.
18. Allemann R. Physical mechanisms contributing to the episodic gas release from Hanford tank 241-SY-101. In: *High Level Radioactive Waste Management*, International High Level Radioactive Waste Management Conference, Las Vegas, USA: American Nuclear Society, 1992.
19. Constantinescu CC, Mukherjee J. Performance evaluation of an Inveon PET preclinical scanner. *Phys Med Biol.* 2009;54(9):2885–2899.
20. Best A, Richardson M, Boudreau B, Judd A, Leifer I, Lyons A, Martens C, Orange D, Wheeler S. Shallow seabed methane gas could pose coastal hazard. *Eos Trans Am Geophys Union.* 2006;87(22):213–217.
21. Maurer S, Gschwend D, Wagner EC, Schildhauer TJ, Ruud van Ommen J,Biollaz SM, Mudde RF. Correlating bubble size and velocity distribution in bubbling fluidized bed based on x-ray tomography. *Chem Eng J.* 2016;298:17–25.
22. D'Orazio F, Tarczon JC, Halperin WP, Eguchi K, Mizusaki T. Application of nuclear magnetic resonance pore structure analysis to porous silica glass. *J Appl Phys.* 1989;65(2):742–751.
23. Yao YB, Liu DM, Cai YD, Li JQ. Advanced characterization of pores and fractures in coals by nuclear magnetic resonance and X-ray computed tomography. *Sci China Earth Sci.* 2010;53(6):854–862.
24. Selomulya C, Tran T, Jia X, Williams R. An integrated methodology to evaluate permeability from measured microstructures. *AIChE J.* 2006;52(10):3394–3400.
25. Gregson CR, Goddard DT, Sarsfield MJ, Taylor RJ. Combined electron microscopy and vibrational spectroscopy study of corroded Magnox sludge from a legacy spent nuclear fuel storage pond. *J Nucl Mater.* 2011;412(1):145–156.
26. Johnson M, Peakall J, Fairweather M, Biggs SR, Harbottle D, Hunter TN. Characterisation of multiple hindered settling regimes in aggregated mineral suspensions. *Ind Eng Chem Res.* 2016;55(37): 9983–9993.
27. Xiao D, Lu Z, Jiang S, Lu S. Comparison and integration of experimental methods to characterize the full-range pore features of tight gas sandstone—a case study in Songliao Basin of China. *J Nat Gas Sci Eng.* 2016;34:1412–1421.
28. Anovitz LM, Cole DR. Characterization and analysis of porosity and pore structures. *Rev Mineral Geochem* 2015;80(1):61–164.
29. Yao Y, Liu D. Comparison of low-field NMR and mercury intrusion porosimetry in characterizing pore size distributions of coals. *Fuel.* 2012;95:152–158.
30. Mahmoodlu M, Raoof A, Sweijen T,van Genuchten MT. Effects of sand compaction and mixing on pore structure and the unsaturated soil hydraulic properties. *Vadose Zo J.* 2016;15(8):0–11.
31. Seland JG, Bruvold M, Brurok H, Jynge P, Krane J. Analyzing equilibrium water exchange between myocardial tissue compartments using dynamical two-dimensional correlation experiments combined with manganese-enhanced relaxography. *Magn Reson Med.* 2007;58(4): 674–686.
32. Matsumoto H, Maki A, Shen JW, Takeuchi H. PM-07A non-linear discrete reconstruction method based on the gray-level quantization unit. *Microscopy.* 2016;65(suppl 1):i35.1–i35.
33. Villinger C, Neusser G, Kranz C, Walther P, Mertens T. 3D analysis of HCMV induced-nuclear membrane structures by FIB/SEM tomography: Insight into an unprecedented membrane morphology. *Viruses.* 2015;7(11):5686–5704.
34. Heindel TJ. A review of x-ray flow visualization with applications to multiphase flows. *J Fluids Eng.* 2011;133(7):1–16.
35. Schindelin J, Arganda-Carreras I, Frise E, Kaynig V, Longair M, Pietzsch T, Preibisch S, Rueden C, Saalfeld S, Schmid B, Tinevez J-Y, White DJ, Hartenstein V, Eliceiri K, Tomancak P, Cardona A. Fiji: an open-source platform for biological-image analysis. *Nat Methods.* 2012;9(7):676–682.
36. Menon M, Yuan Q, Jia X, Dougill AJ, Hoon SR, Thomas AD, Williams RA. Assessment of physical and hydrological properties of biological soil crusts using X-ray microtomography and modeling. *J Hydrol.* 2011;397(1–2):47–54.
37. Ning R, Tang X, Conover D. X-ray scatter correction algorithm for cone beam CT imaging. *Med Phys.* 2004;31(5):1195–1202.
38. Bentz DP, Quenard DA, Kunzel HM, Baruchel J, Peyrin F, Martys NS, Garboczi EJ. Microstructure and transport properties of porous building materials. I1: three-dimensional X-ray tomographic studies. *Mater Struct.* 2000;33(3):147–153. (April):
39. Ketcham R, Carlson WD. Acquisition, optimization and interpretation of x-ray computed tomographic imagery: applications to the geosciences. *Comput Geosci.* 2001;27(4):381–400.
40. Boden S, Bieberle M, Hampel U. Quantitative measurement of gas hold-up distribution in a stirred chemical reactor using X-ray cone-beam computed tomography. *Chem Eng J.* 2008;139(2):351–362.
41. Bolte S, Cordelières FP. A guided tour into subcellular colocalization analysis in light microscopy. *J Microsc.* 2006;224(Pt 3):213–232.
42. Katsman R. Correlation of shape and size of methane bubbles in fine-grained muddy aquatic sediments with sediment fracture toughness. *J Struct Geol.* 2015;70:56–64.
43. Algar CK, Boudreau BP. Stability of bubbles in a linear elastic medium: Implications for bubble growth in marine sediments. *J Geophys Res Earth Surf.* 2010;115(F3):F03012
44. Li M, Wilkinson D. Determination of non-spherical particle size distribution from chord length measurements. Part 1: theoretical analysis. *Chem Eng Sci.* 2005;60(12):3251–3265.
45. Lawson C, Hanson R. *Solving Least Squares Problems*. Englewood Cliffs, NJ: Prentice-Hall, 1974.
46. Lin C, Videla A, Miller J. Advanced three-dimensional multiphase flow simulation in porous media reconstructed from X-ray Microtomography using the HeChenZhang Lattice Boltzmann Model. *Flow Meas Instrum.* 2010;21(3):255–261.
47. Moreno-Atanasio R, Williams RA, Jia X. Combining x-ray microtomography with computer simulation for analysis of granular and porous materials. *Particuology.* 2010;8(2):81–99.
48. Guadarrama-Lara R, Jia X, Fairweather M. A meso-scale model for fluid-microstructure interactions. *Procedia Eng.* 2015;102:1356–1365.
49. Guan Y, Guadarrama-Lara R, Jia X, Zhang K, Wen D. Lattice Boltzmann simulation of flow past a non-spherical particle. *Adv Powder Technol.* 2017;28(6):1486–1494.
50. Succi S. *The Lattice Boltzmann Equation: For Fluid Dynamics and Beyond*. Oxford: Oxford University Press, 2001.
51. Quispe JR, Rozas RE, Toledo PG. Permeability porosity relationship from a geometrical model of shrinking and lattice Boltzmann and Monte Carlo simulations of flow in two-dimensional pore networks. *Chem Eng J.* 2005;111(2–3):225–236.
52. Jia X, Wedlock DJ, Williams RA. Simulation of simultaneous aggregation and sedimentation. *Miner Eng.* 2000;13(13):1349–1360.
53. Abbasi H, Evans JW, Abramson IS. Diffusion of gases in porous solids: Monte Carlo simulations in the Knudsen and ordinary diffusion regimes. *AIChE J.* 1983;29(4):617–624.
54. Evans JW, Abbasi MH, Sarin A. A Monte Carlo simulation of the diffusion of gases in porous solids. *J Chem Phys.* 1980;72(5): 2967–2973.

55. Zalc M, Reyes C, Iglesia E. Monte-Carlo simulations of surface and gas phase diffusion in complex porous structures. *Chem Eng Sci.* 2003;58(20):4605–4617.
56. Laudone GM, Matthews GP, Gane PAC. Modelling diffusion from simulated porous structures. *Chem Eng Sci.* 2008;63(7):1987–1996.
57. Crank J. *The Mathematics of Diffusion*. London: Oxford university press, 1979.
58. Winter E. Diffusion properties of gases: part IV—the self-diffusion coefficients of nitrogen oxygen and carbon dioxide. *Trans Faraday Soc.* 1951;47(0):342–347.
59. Reichenbacher W, Müller P, Klemm A. Diffusion von HT, DT und T2 in H2 und D2 bei. *Z Naturforschg.* 1965;20:24C–1536. 1529
60. Kam S, Rossen W. Anomalous capillary pressure, stress, and stability of solids-coated bubbles. *J Colloid Interface Sci.* 1999;213(2):329–339.
61. Terrones G, Gauglitz PA. Deformation of a spherical bubble in soft solid media under external pressure. *Q J Mech Appl Math.* 2003;56(4): 513–525.
62. Wheeler S, Sham W, Thomas S. Gas pressure in unsaturated offshore soils. *Can Geotech J.* 1990;27(1):79–89. 1989
63. Jain AK, Juanes R. Preferential mode of gas invasion in sediments: grain-scale mechanistic model of coupled multiphase fluid flow and sediment mechanics. *J Geophys Res Solid Earth.* 2009;114(B8):B08101.
64. Anderson AL, Abegg F, Hawkins JA, Duncan ME, Lyons AP. Bubble populations and acoustic interaction with the gassy floor of Eckernforde Bay. *Cont Shelf Res.* 1998;18(14–15):1807–1838.
65. Ransohoff TC, Gauglitz PA, Radke CJ. Snap-off of gas bubbles in smoothly constricted noncircular capillaries. *AIChE J.* 1987;33(5):753–765.
66. Withers PJ. Fracture mechanics by three-dimensional crack tip synchrotron x-ray microscopy. *Philos Trans A.* 2015;373:20130157.
67. Burghard HC. The influence of precipitate morphology on microvoid growth and coalescence in tensile fractures. *Metall Trans.* 1974;5(9): 2083–2094.
68. Reynolds CA, Menke H, Andrew M, Blunt MJ, Krevor S. Dynamic fluid connectivity during steady-state multiphase flow in a sandstone. *Proc Natl Acad Sci.* 2017;114(31):8187–8192.
69. Wu M, Cheng Z, Wu J, Wu J. Precise simulation of long-term DNAPL migration in heterogeneous porous media based on light transmission micro-tomography. *J Environ Chem Eng.* 2017;5(1): 725–734.
70. Krieger IM, Mulholland GW, Dickey CS. Diffusion coefficients for gases in liquids from the rates of solution of small gas bubbles. *J Phys Chem.* 1967;71(4):1123–1129.
71. Boudreau BP. The physics of bubbles in surficial, soft, cohesive sediments. *Mar Pet Geol.* 2012;38(1):1–18.
72. Bear J. *Dynamics of Fluids in Porous Media. Dover Civil and Mechanical Engineering Series*. New York: Dover Publications Inc., 1972.
73. Hirschfelder JO, Curtiss CF, Bird RB. *Molecular Theory of Gases and Liquids*. New York: John Wiley & Sons, Inc., 1954.
74. Winterwerp JC, van Kesteren WGM. Introduction to the physics of cohesive sediment dynamics in the marine environment. In: van Loon T, editor, *Developments in Sedimentology*, Vol. 56. Amsterdam: Elsevier; 2004:397–428.
75. Berg S, Ott H, Klapp SA, Schwing A, Neiteler R, Brussee N, Makurat A, Leu L, Enzmann F, Schwarz JO, Kersten M, Irvine S, Stampanoni M. Real-time 3D imaging of Haines jumps in porous media flow. *Proc Natl Acad Sci USA.* 2013;110(10):3755–3759.
76. Gauglitz PA, Radke CJ. Dynamics of Haines jumps for compressible bubbles in constricted capillaries. *AIChE J.* 1989;35(2):230–240.
77. Liu L, Kock TD, Wilkinson J, Cnudde V, Xiao S, Buchmann C, Uteau D, Peth S, Lorke A. Methane bubble growth and migration in aquatic sediments observed by micro-scale X-ray computed tomography. *Environ Sci Technol.* 2018;52(4):2007–2015.
78. Gauglitz PA, Bontha JR, Daniel RC, Mahoney LA, Rassat SD, Wells BE, Bao J, Boeringa GK, Buchmiller WC, Burns CA. *Hydrogen Gas Retention and Release from WTP Vessels: Summary of Preliminary Studies, Vol.* 24255. Richmond, WA: Pacific Northwest National Laboratory, 2015.

Manuscript received Jan. 18, 2018, and revision received May. 24, 2018.